Study of upward-going muons in Super-Kamiokande

Choji Saji

Doctral Program in Fundamental Science and Energy Technology
Graduate School of Science and Technology
Niigata University

Acknowledgement

First of all, I would like to express my great appreciation to my adviser, Prof. Kazumasa Miyano. He introduced me to experimental physics and encouragement, Without his excellent support and encouragement, this thesis would never have been completed.

I would like to thank Prof. N.Tamura and Prof. H.Miyata. They always encouraged and supported me.

I acknowledge Prof. Y.Totsuka, spokesman of the Super-Kamiokande experiments. He gave me the opportunity to participate in such an enthusiastic time of the study of the neutrino oscillation.

I am deeply indebted to members of upward-going muon analysis group. Especially I would like to thank Dr. M.Takita. His many instructive suggestion and encouragement were indispensable to progress this study. I would like to thank Dr. A.Okada, Dr. M.Takahata, Dr. M.Yoshida and Mr. K.Nitta. And also wish to thank the members in USA, Prof. R.J.Wilkes, Prof. J.G.Learned, Dr. A.Habig, Dr. S.Matsuno, Dr. A.L.Stachyra and Mr. D.Shantanu.

I would like to thank all the Super-Kamiokande collaborators for help with the experiments.

At last, I would like to thank all graduate students in High Energy Physics group at Niigata university.

Abstract

Upward-going muons produced in the surrounding rock by high energy atmospheric neutrinos have been measured for using the large underground water Cherenkov detector, Super-Kamiokande. During about 1250days data was studied. The experimental upward-going muon flux was obtained. The expected upward-going muon flux was estimated by analytical calculation and Monte Carlo method, respectively.

The $\nu_\mu \to \nu_\tau$ vacuum oscillation is considered as the most probable process. The $\nu_\mu \to \nu_\tau$ oscillation hypothesis with $\sin^2 2\theta \geq 0.65, 1.9 \times 10^{-3} \leq \Delta m^2 \leq 7.2 \times 10^{-3}$ is consistent with the observed zenith angle shape at 90% confidence level.

The observed atmospheric $\nu_\mu/\bar{\nu_\mu}$ ratio was measured and the expected ratio was estimated by analytical calculation. The ratio of observed to expected was $0.29^{+0.39}_{-0.29}(\text{stat.}) \pm 0.04(\text{syst.})$ obtained.

Contents

List of Figures

List of Tables

Chapter 1

Introduction

1.1 Neutrino oscillation

The neutrino is one of leptons that are classified into three types, electron, muon and tau type. Each type has its own anti-particle. Neutrinos have no charge and are thought to have zero mass in the standard model. However, there are essentially unsolved problems in neutrino masses. If neutrinos are indeed massive, then neutrino oscillation may be observed. The oscillation probability, for which one neutrino changes its flavor into another depends on the mass-squared difference of the two neutrino mass eigenstates(Δm^2) and the mixing angle parameter(θ).

We give a brief review of the neutrino oscillations. The observed neutrinos, $|\nu_\mu\rangle$ and $|\nu_\tau\rangle$, are flavor eigenstates and the massive neutrinos, $|\nu_1\rangle$ and $|\nu_2\rangle$, are the mass eigenstates, respectively. The relation between the flavor eigenstates and the mass eigenstates with the transformation matrix, U, is written by,

$$\begin{pmatrix} \nu_\mu \\ \nu_\tau \end{pmatrix} = U \begin{pmatrix} \nu_1 \\ \nu_2 \end{pmatrix} = \begin{pmatrix} \cos\theta & \sin\theta \\ -\sin\theta & \cos\theta \end{pmatrix} \begin{pmatrix} \nu_1 \\ \nu_2 \end{pmatrix} \tag{1.1}$$

where θ is the mixing angle in vacuum. Time evolution of a state $\nu(t)$ is written as,

$$i\frac{d}{dt}\nu_j(t) = E_j\nu_j(t) \quad (j = 1, 2), \tag{1.2}$$

where E_j is the energy of ν_j, j is the index of mass eigenstates. The neutrino wave function is written as,

$$\begin{pmatrix} \nu_1(t) \\ \nu_2(t) \end{pmatrix} = \begin{pmatrix} \exp(-iE_1t) & 0 \\ 0 & \exp(-iE_2t) \end{pmatrix} \begin{pmatrix} \nu_1(0) \\ \nu_2(0) \end{pmatrix}, \tag{1.3}$$

where $\nu_1(0)$ and $\nu_2(0)$ are the mass eigenstates at $T = 0$ and $\nu_1(t)$ and $\nu_2(t)$ are at $T = t$. Eq. 1.3 is rewritten using Eq. 1.1 as,

$$\begin{pmatrix} \nu_\mu(t) \\ \nu_\tau(t) \end{pmatrix} = U \begin{pmatrix} \exp(-iE_1t) & 0 \\ 0 & \exp(-iE_2t) \end{pmatrix} U^\dagger \begin{pmatrix} \nu_1(0) \\ \nu_2(0) \end{pmatrix}, \tag{1.4}$$

The probability that a neutrino ν_μ remains to be ν_μ is written as,

$$P(\nu_\mu \to \nu_\mu) = \left| \begin{pmatrix} 1 & 0 \end{pmatrix} U \begin{pmatrix} \exp(-iE_1 t) & 0 \\ 0 & \exp(-iE_2 t) \end{pmatrix} U^\dagger \begin{pmatrix} 1 \\ 0 \end{pmatrix} \right|^2 \tag{1.5}$$

$$= \left| \exp(-iE_1 t)\cos^2\theta + \exp(-iE_2 t)\sin^2\theta \right|. \tag{1.6}$$

If neutrino mass is sufficiently smaller than their momentum, the following approximation can be applied,

$$E_j \approx p + \frac{m_j^2}{2p}, \tag{1.7}$$

where m_j is the mass of neutrino ν_j and p is the momentum of ν_μ. Finally, the survival probability can be written as:

$$P(\nu_\mu \to \nu_\mu) = 1 - \sin^2 2\theta \sin^2\left(\pi \frac{L}{L_\nu}\right) \tag{1.8}$$

where $\Delta m^2 = m_2^2 - m_1^2(\mathrm{eV}^2)$, and $L(\mathrm{km})$, L_ν are the path length and oscillation length of neutrino, respectively. L_ν is defined as,

$$L_\nu = 2.48(\mathrm{km}) \times \frac{p_\nu}{\Delta m^2} \tag{1.9}$$

where p_ν is neutrino momentum in GeV.

Chapter 2

Atmospheric neutrino

In this chapter, we report atmospheric neutrino and one detected by Super-Kamiokande detector.

2.1 Atmospheric neutrino production

The cosmic-ray incident on the atmosphere consists of protons and nuclei. High energy cosmic-ray interacts with the atmosphere whose major components are oxygen and nitrogen, and some kinds of mesons are generated at the altitude of about 10km hight in the atmosphere. These mesons produce eventually some neutrinos which are called as the atmospheric neutrinos. The mesons decay as follows,

$$\begin{array}{lcllll}
\pi^{\pm} & \rightarrow & \mu^{\pm} & \nu_{\mu}(\bar{\nu}_{\mu}) & & \\
\mu^{\pm} & \rightarrow & e^{\pm} & \nu_{e}(\bar{\nu}_{e}) & \bar{\nu}_{\mu}(\nu_{\mu}) & \\
K^{\pm} & \rightarrow & \mu^{\pm} & \nu_{\mu}(\bar{\nu}_{\mu}) & & \\
 & \rightarrow & \pi^{0} & \mu^{\pm} & \nu_{\mu}(\bar{\nu}_{\mu}) & \\
 & \rightarrow & \pi^{0} & e^{\pm} & \nu_{e}(\bar{\nu}_{e}) & \\
K_{L}^{0} & \rightarrow & \pi^{\pm} & \mu^{\pm} & \nu_{\mu}(\bar{\nu}_{\mu}) & \\
 & \rightarrow & \pi^{\pm} & e^{\pm} & \nu_{e}(\bar{\nu}_{e}) &
\end{array}$$

Because of rapidly decay of kaons, the kaon decay is important in the higher energy region.

The uncertainty in the calculation of atmospheric neutrino flux is estimated to be about 20%, due to the uncertainties in the flux of the primary cosmic-ray and hadronic interactions.

2.2 Atmospheric neutrino in Super-Kamiokande

The atmospheric neutrino generated in the atmosphere propagates to the detector in the earth and interacts with water in the detector or rock out of the detector, then

electrons, muons and pions are produced by charged current interaction or neutral current interaction. The contained event is detected as Cherenkov light by these muons and pions. Atmospheric neutrinos detected by Super-Kamiokande can be categorized as follows,

- Contained event
  A contained event is categorized by event topology and also reflects parent neutrino energy as follows,

  1. Fully contained event
     The interaction point of the neutrino is inside the detector, and the generated particle stops within the fiducial volume of the detector. The neutrino grouped into this category has about 1 GeV energy.
  2. Partially contained event
     The interaction point of the neutrino is inside the detector, and generated particle goes out of the detector. The neutrino grouped into this category has about 5$\sim$ 10GeV energy.

- Upward-going muon event
  Atmospheric neutrinos generated on the opposite side of the earth can propagate through it and interact with rock surrounding the detector. If the interaction region is within about 5km, the muons generated by charged current interaction may penetrate the rock to the detector. Muons induced by such neutrinos are observed having upward-going direction(Fig. 2.1).
  The upward-going event is categorized by detecting topology as follows,

  1. Upward through-going muon event
     The muon events which come from underneath the detector generated in the rock. The muon goes through the whole detector. Fig.2.2 is a typical upward through-going muon event.
  2. Upward stopping muon event
     The muon events which come from underneath the detector generated in the rock. The muon crosses the detector partially and stops in the detector. Fig.2.3 is a typical upward stopping muon event.

2.3 Upward-going muon in Super-Kamiokande

Almost all downward-going muons are cosmic-ray muons which are generated directly in the atmosphere. Downward-going muons penetrate into the detector but cannot be distinguished muons induced from neutrinos. Therefore, we select only muons going upward. Electron neutrinos also interact with rock and upward going electrons can be

generated. However, they produce showers in the rock and the track length is too short to reach at the detector.

The average energy of the parent neutrino for these events is about 10GeV for upward stopping muons and 100GeV for upward through-going muons. The energy distributions for stopping muons, through-going muons and sum of them are shown in Fig.2.4. According to the figure, the energy region of parent neutrinos for stopping muons is about 1.6GeV to 100GeV. For through-going muons, it is a few GeV to over 10TeV.

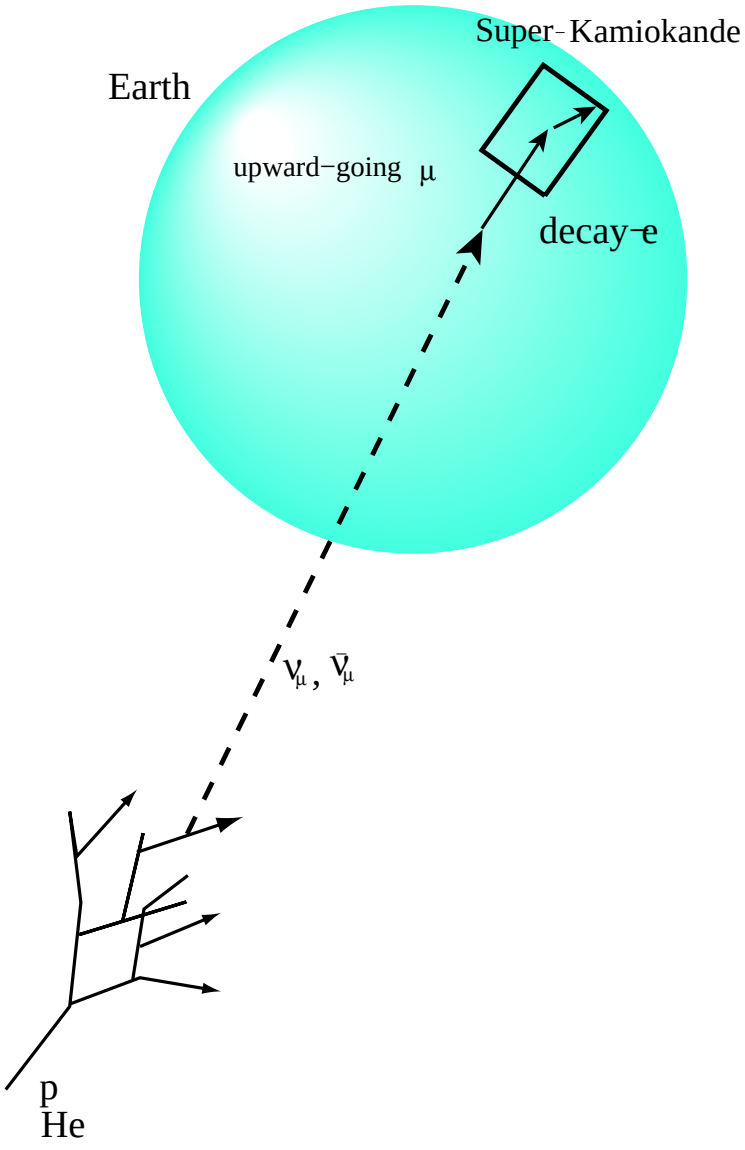

Figure 2.1: Schematic view of upward going muon event

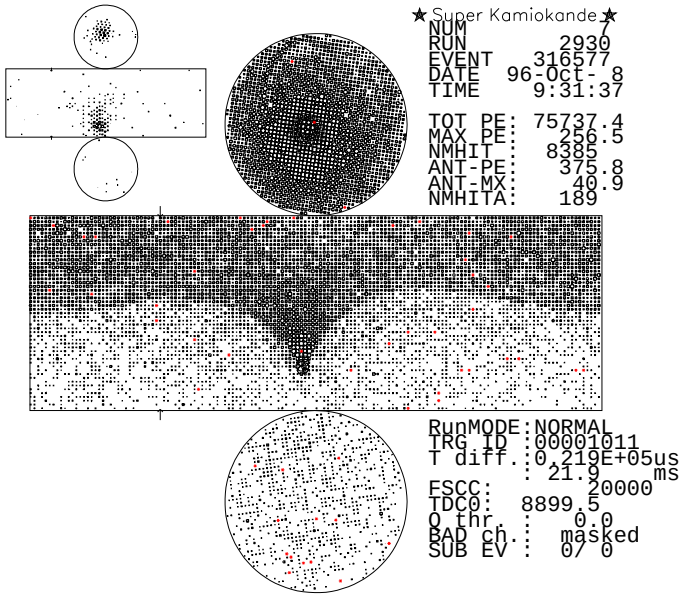

Figure 2.2: The typical event for upward through-going muon event
the larger display is inner-detector and the smaller display is outer-detector

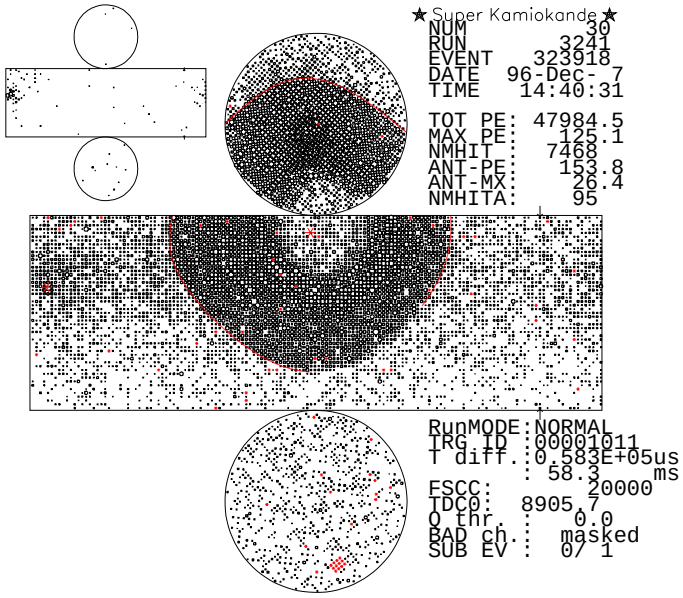

Figure 2.3: The typical event for upward stopping muon event

If neutrinos actually oscillate, the observed upward-going muon flux will deviate from expectation and Δm^2 and mixing angle will not be zero. Since the survival probability depends on neutrino energy E_ν and path length L, because the flux of muon neutrinos in the energy region from a few GeV up to over 10TeV can be searched, upward-going muon

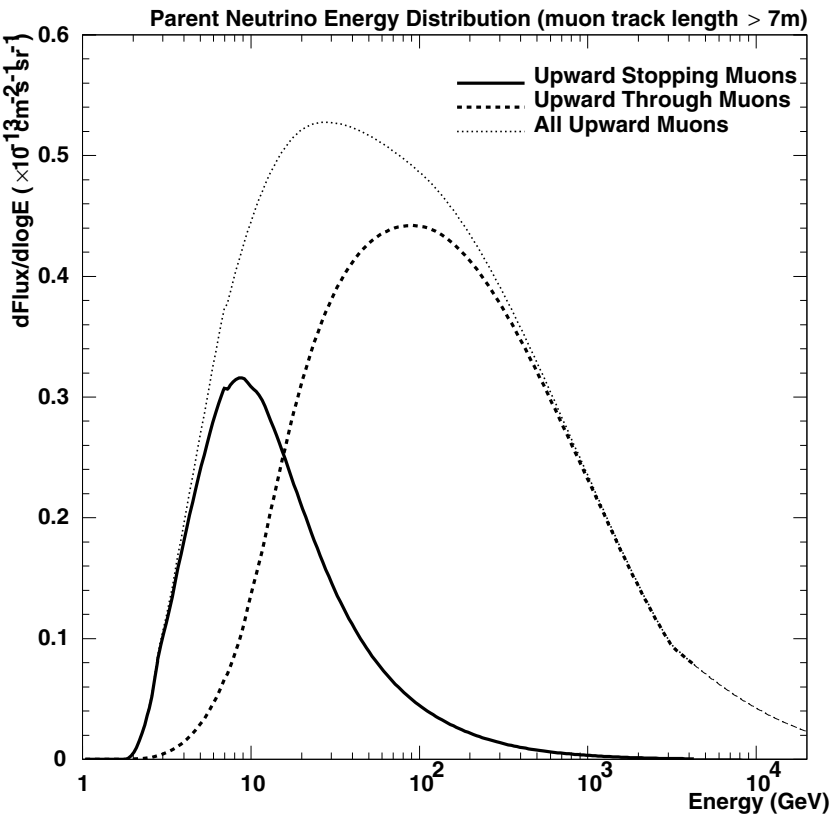

Figure 2.4: Energy distribution of parent neutrino for upward muons. All upward muons mean sum of stopping muon and through-going muon.

is suitable for oscillation study. As a consequence of oscillations, the flux of upward-going muons should be affected both in the absolute number of events and in the shape of the zenith angle distribution, with relatively fewer observed events near the vertical than near the horizontal. This is due to the longer path length of neutrinos from production point to their observation point.

Chapter 3

Super-Kamiokande detector

The major themes of this detector are experiments on nucleon decay and on neutrino detection. Super-Kamiokande is located a depth of 2700meters water equivalent in the Kamioka Observatory in Japan, near the Kamiokande. The schematic view of Super-Kamiokande is shown in Fig.3.1. Super-Kamiokande is a cylindrical 50 kton water Cherenkov image detector. It started running in April 1996.

Since the detector is located deep under ground, the cosmic-ray muon background is reduced. The intensity of cosmic-ray muons at the surface of the earth is about $10^9 \mathrm{m}^{-2}\mathrm{y}^{-1}$. In the Kamioka mine, the intensity is reduced to 10^{-5}. The lowest energy of cosmic-ray muons detected by Super-Kamiokande is about 1.3TeV. The atmospheric muon rate at Super-Kamiokande is about 2.2Hz. The properties of the Super-Kamiokande are given briefly shown in Table 3.1. Especially important characteristics are as follows,

1. Due to its large volume, it is suitable for nucleon decay experiment and neutrino detection experiment.

2. A charged particle's vertex position, direction, and momentum can be reconstructed

3. A charged particles e, μ, π can be identified.

4. It was good energy resolution with 40% photosensitive coverage of large diameter PMTs.

5. Since the optical separation between the inner and outer detectors is almost complete, the detector can separate between neutral particles coming from outside of the tank and charged particles generated by interaction inside the tank.

3.1 Water Cherenkov image counter

The Super-Kamiokande is a ring-imaging water Cherenkov detector. The detector detects Cherenkov photons emitted in water by charged particles. When the velocity of the

	Super-Kamiokande	remark
Total size	42mh × 39mϕ	
Total volume	50,000t	
Number of PMTs	11,146(50cmϕ) 1,885(20cmϕ)	inner-detector outer-detector
Photosensitive coverage	40%	
Timing resolution for PMT	3nsec	at 1 photo-electron
Energy resolution	2.6% / $\sqrt{E}$ 2.5% 16% / $\sqrt{E}$	e(E(GeV)) μ ($<$ 1GeV) e ($<$ 20MeV)
Vertex resolution	50cm $\sim$ 10cm	e (10MeV) $p \rightarrow e^{+}\pi^{0}$
Angular resolution	28° $\sim 1°$	e (10MeV) through going μ
Trigger threshold energy Analytical threshold energy	$4 \sim 5$MeV 5MeV	
e/μ separation	99%	$0.03 < p_e < 1.33$GeV/c $0.2 < p_\mu < 1.5$GeV/c

Table 3.1: Specification and performance of the Super-Kamiokande detector

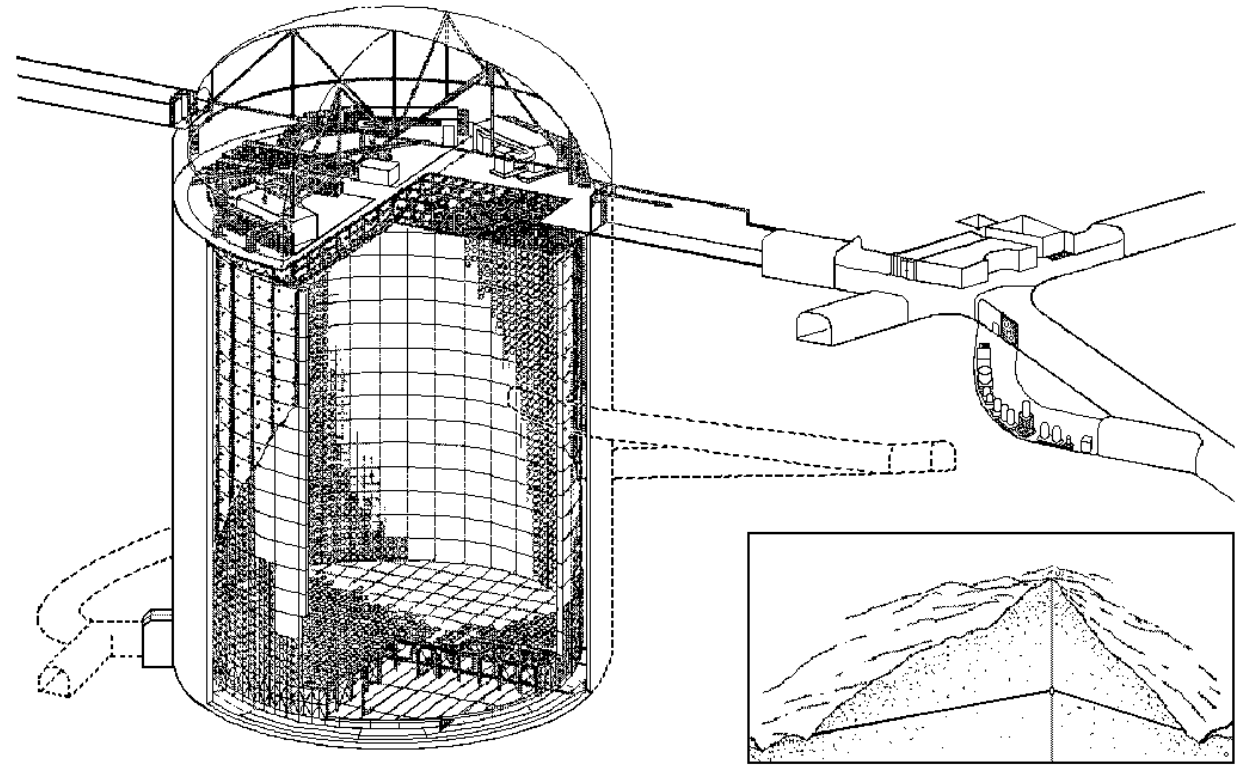

Figure 3.1: Schematic view of Super-Kamiokande

charged particle β exceed the speed of light in the de-electric medium, a charged particle emits Cherenkov photons. If n is the refraction index of the medium, then

$$n\beta \geq 1, \beta = v/c \tag{3.1}$$

Cherenkov photons are emitted forward like a circular cone with a half opening angle θ to the direction of motion of the particle(3.2). The opening angle θ is related to n, β as follows,

$$\cos\theta = \frac{1}{n\beta} \tag{3.2}$$

In this experiment the medium is water($n = 1.33$) and the emitted Cherenkov light is detected by PMTs. The critical energy of each charged particle for Cherenkov light emission is shown in Table 3.2

Particle	Critical energy(MeV)
$e^{\pm}$	0.766
$\mu^{\pm}$	157.4
$\pi^{\pm}$	207.9
$K^{\pm}$	735.5

Table 3.2: Critical energy for Cherenkov light emission in water

The maximum emission angle of Cherenkov light is about 42° at $\beta = 1$. The number of photons emitted per unit path length per wave length is,

$$\frac{d^2N}{dxd\lambda} = 2\pi Z^2\alpha(1 - \frac{1}{n^2\beta^2})\frac{1}{\lambda^2} \tag{3.3}$$

x : path length
λ : wave length of Cherenkov light
N : number of photon
α : fine structure constant(1/137)
Z : Charge of particle

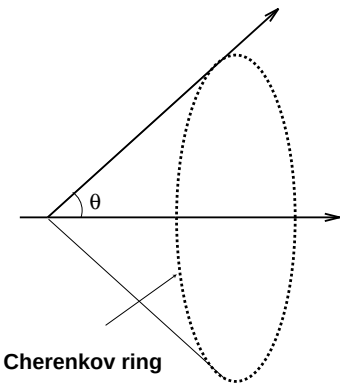

Figure 3.2: Cone of Cherenkov light

3.2 Detector components

The tank of the Super-Kamiokande detector is 41.4m in height and 39.3m in diameter and the cavity is coated with about 50cm thick concrete and is covered with 8mm thick stainless steel water-tightly. This tank is filled with 50,000m^3 ultra pure water.

The PMTs are located on the stainless structure(Fig.3.3), 11146 PMTs in the inner-detector and 1885 PMTs in the outer-detector. The size of PMT is 50cm in diameter in the inner-detector and 20cm in the outer-detector. Inner-detector and outer-detector are optically separated by black sheet(Fig.3.3). The inner-detector is used for particle detection while the outer-detector vetoes incoming events from outside of the detector. The high voltage supply and the data acquisition system are located on the top of the detector.

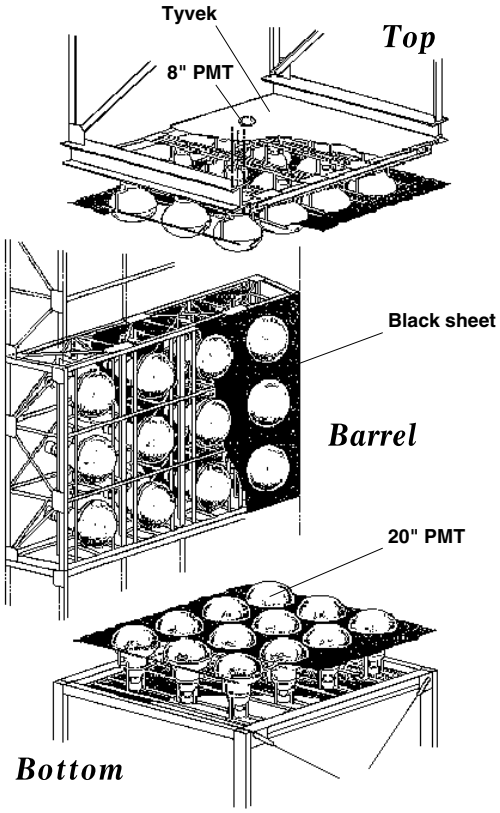

Figure 3.3: The structure of the frame for PMTs

3.3 PMTs

The PMT was developed by HAMAMATSU Photonics Company for the Super-Kamiokande experiment(Fig.3.4). As described earlier, two types of PMTs which differ in diameter are installed in the inner and outer detectors.

- Inner 20-inch ϕ PMT
  The photo-multiplier tubes in Super-Kamiokande are improved version of the PMTs

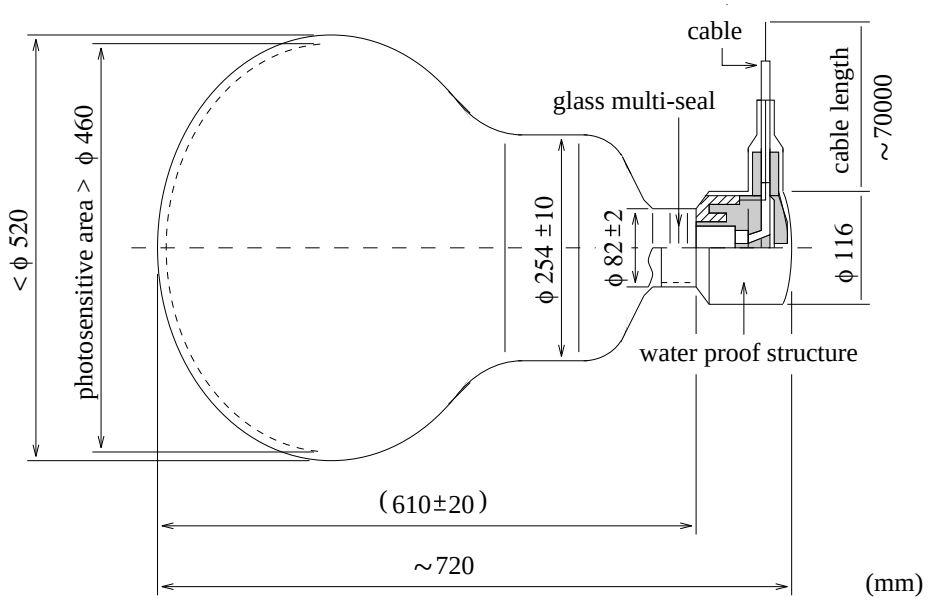

Figure 3.4: 20inch PMT

in Kamiokande which were also developed by HAMAMATSU Photonics CO. LTD. With several improvements in the dinode shape and the bleeder chain were carried out, we obtained good timing and energy resolution. Timing resolution is improved from 3nsec in Kamiokande to 2nsec (Fig. 3.5). These improvements affect many low energy event analysis and we obtain even better energy and vertex resolution.

The quantum efficiency and the spectrum of Cherenkov light are shown in Fig.3.6. At the peak of the Cherenkov light($\lambda = 390$nm) quantum efficiency is 22%.

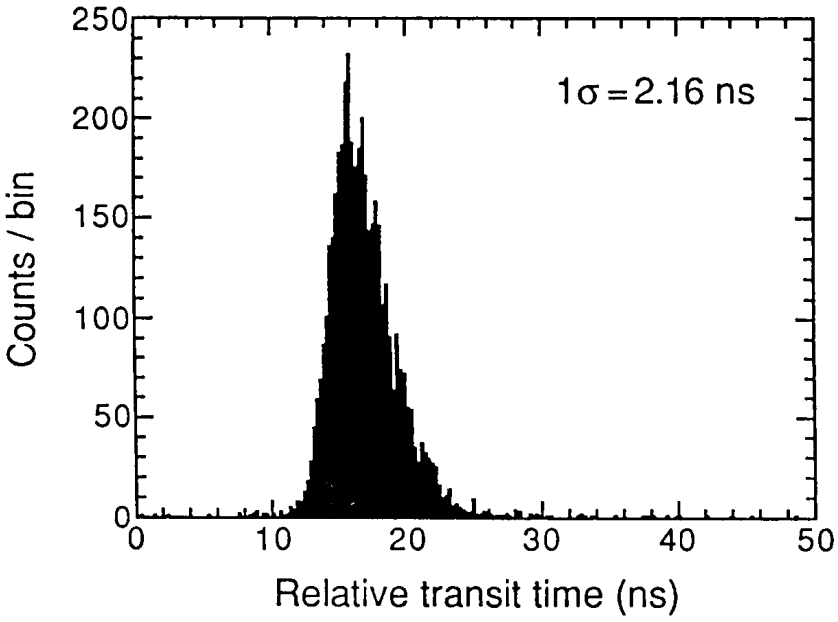

Figure 3.5: The time resolution for 50cm-diameter PMT

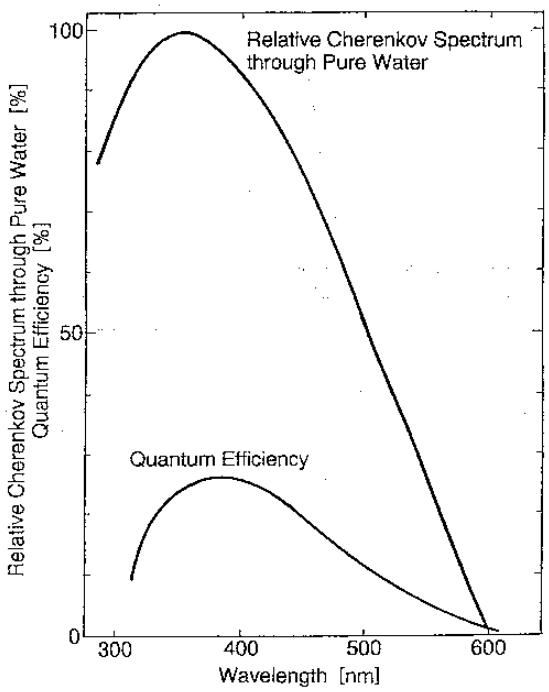

Figure 3.6: Quantum efficiency and spectrum of Cherenkov light

Fig. 3.7 shows a typical pulse height distribution for 1p.e. This figure shows two signals, dark noise(around ADC=0) and signal(around ADC=400), which are clearly divided. Therefore the energy threshold can be decreased to 5MeV. Since electric

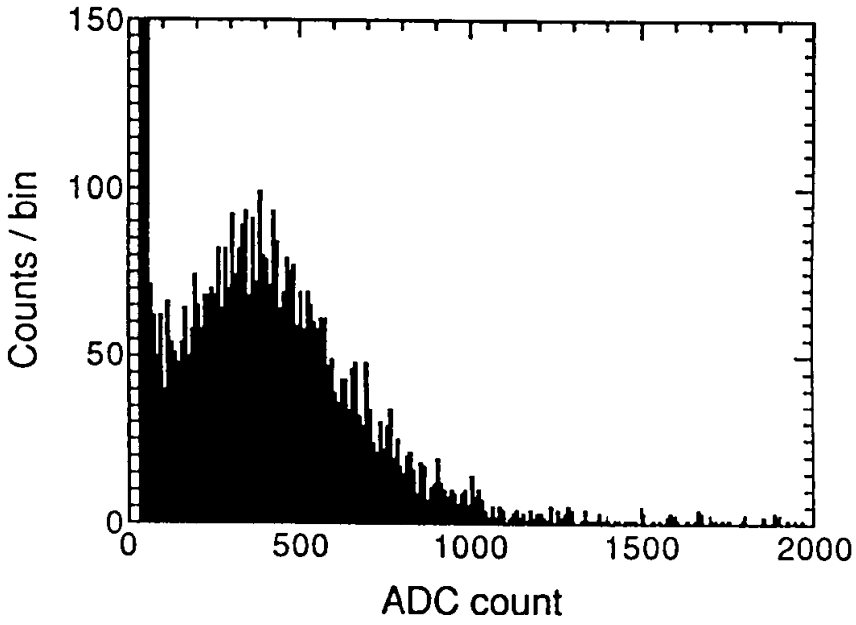

Figure 3.7: A typical 1p.e distribution

wires are laid on the surface of the cavity around the detector, the geomagnetic field is compensated to less than 100G (Fig.3.8)

- Outer 20cm ϕ PMT
  20cm-diameter PMTs are installed to the outer-detector. In order to increase light collection efficiency, PMTs are attached to a 60cm $\times$ 60cm wavelength shifter plate.

3.4 Data acquisition system

Five electronics huts for data acquisition are located on the detector top. Four of these huts are for data taking and power supply and one hut controls the event trigger. At first, one-fourth parts of signal send to workstation in four huts. Next, four parts of data are gathered to control hut and reconstruct to a whole event.

An ATM (Analogue Timing Module) is installed to obtain energy and timing information(Fig.3.9). One ATM deals with signal channels for 12 PMTs and these channels are independent each other. Each channel consists of discriminator, amplifier, ADC(Analogue to Digital converter), TDC(Timing to Digital Converter) and memory. Fig.3.10 is the schematic view of the inner detector data taking system. The inner detector consists of eight parts and each part works independently. One part consists of one workstation, one VME crate, and six TKO boxes. A signal exceeding the threshold is stored in the

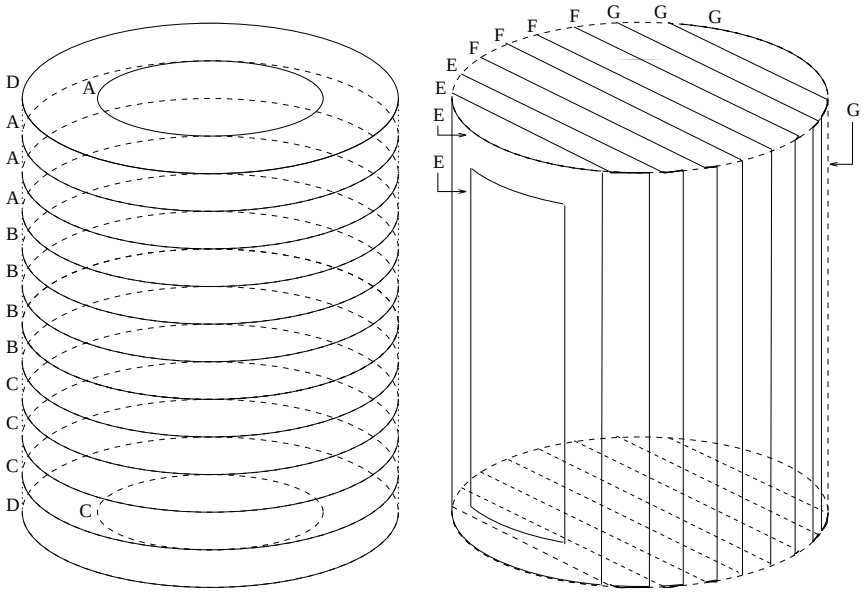

coil	current (A)
A	31.35
B	31.35
C	31.35
D	28.20
E	30.10
F	28.60
G	30.10

Figure 3.8: The coil to compensate for the magnetic field

ATM buffer. When a trigger signal from discriminator is available within 1.2μsec, the stored signal in the ATM buffer is summed. The summed signal is called 'HITSUM' and is treated as global trigger. When this global trigger is available, ADC receives timing, and charge information from the ATM and digitizes them. The digitized signal is received by FIFO(First In First Out). Since both the short digitizing time with about 5μsec and two independent same digitizing systems are performed, the Super-Kamiokande detector achieves the dead time free system. The dead time free system is suitable to collect multiple reaction like proton decay event and successive event in short time like μ decay electron events.

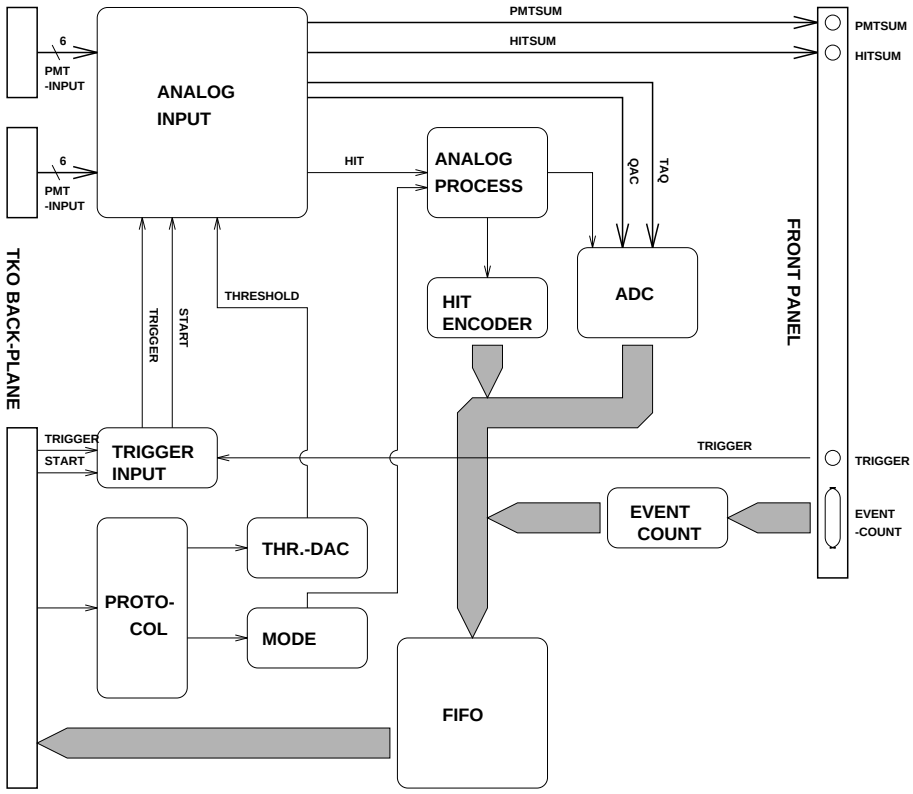

Figure 3.9: Block diagram of the ATM module

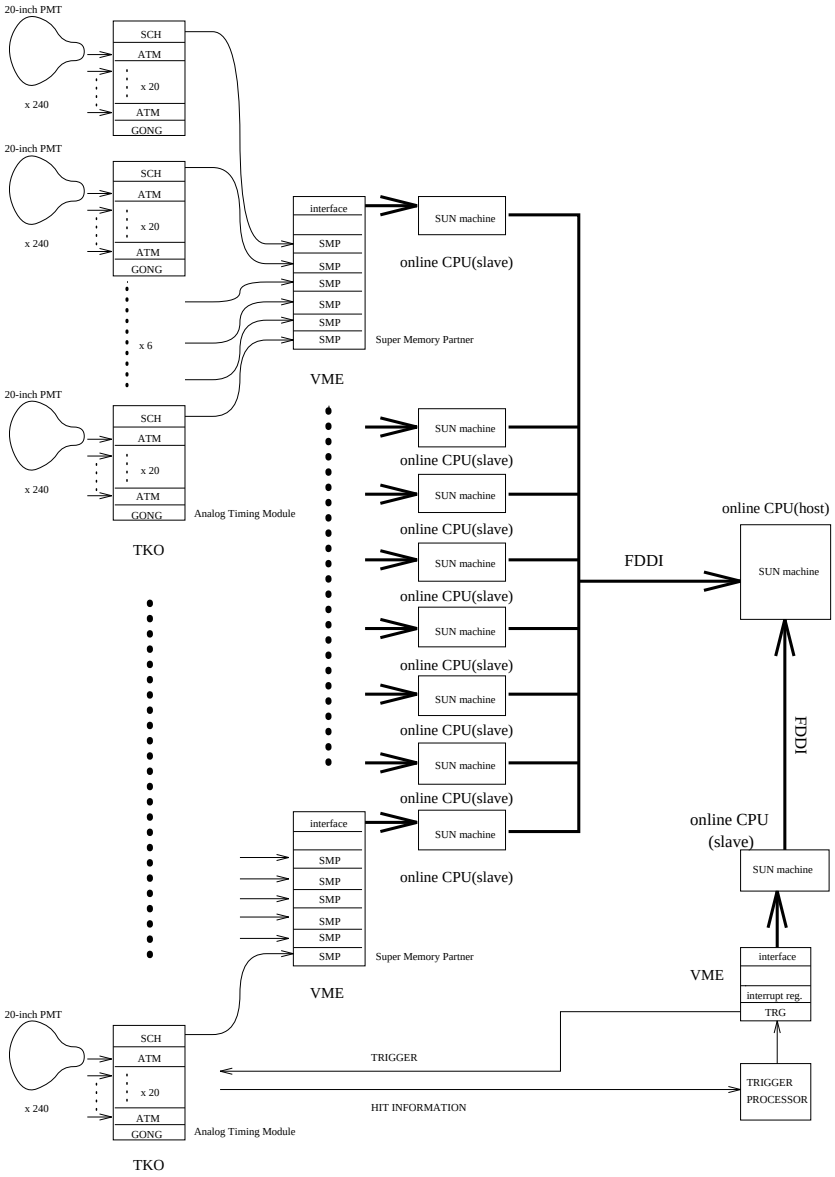

Figure 3.10: Data acquisition system

Chapter 4

Calibration

4.1 Calibration of PMTs

Since many PMTs are used to detect Cherenkov light in Super-Kamiokande detector, energy and timing calibrations are especially important. We describe the relative energy calibration in following section.

The relative energy calibration is done to obtain the same and adjust the gain for each PMT so as to output pulse height from each PMTs. Fig.4.1 shows schematic view of relative energy calibration system.

In relative energy calibration a scintilator ball is used for a light source, because the property of scintilator ball is in good agreement with Cherenkov lights. The relative energy calibration is done by measuring the charge of each PMTs induced by the light of scintilator ball. The position of scintilator ball is changed vertically in order to calibrate at various height. In addition, the correction for the acceptance from the light angle injected to PMTs, the distance between scintilator ball and PMT, and a variation for intensity of light from the Xe lamp are considered. The variation of the gain for each PMTs is adjusted so as to have a uniform gain for PMTs by high-voltage adjustment of each PMTs. The result for the gain adjustment is shown in Fig.4.2. From Fig.4.2 the gain variation after the high-voltage adjustment was estimated to be 7%.

4.2 Calibration for low energy events

The absolute energy calibration is also important in order to reduce systematic error for total energy measurement. Therefore it is required to calibrate the energy within a few percent.

4.2.1 Calibration using neutron capture with Ni

The schematic view is shown in Fig. 4.3. This calibration uses nickel(Ni) for γ source,

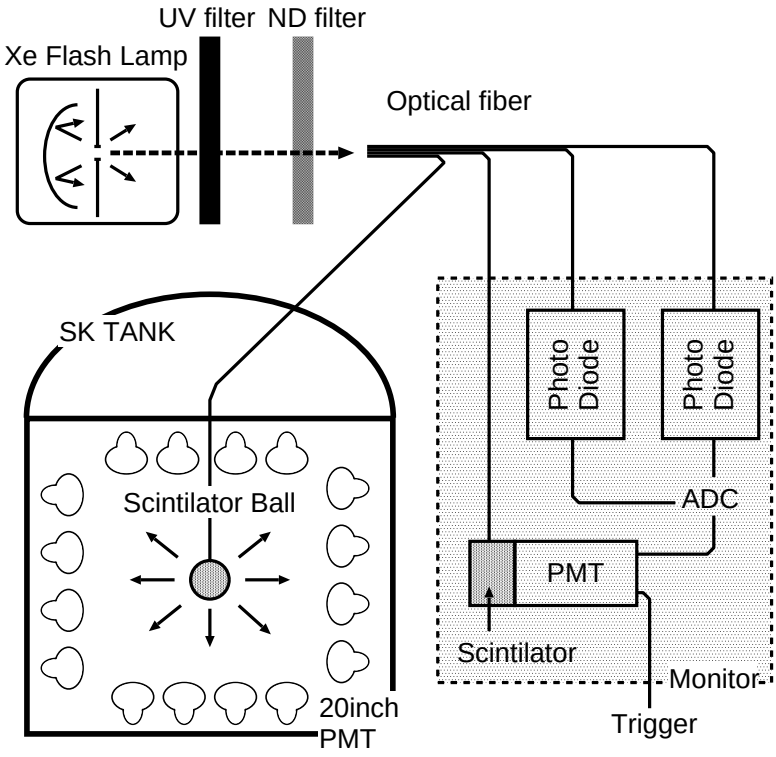

Figure 4.1: Schematic view of relative energy calibration system

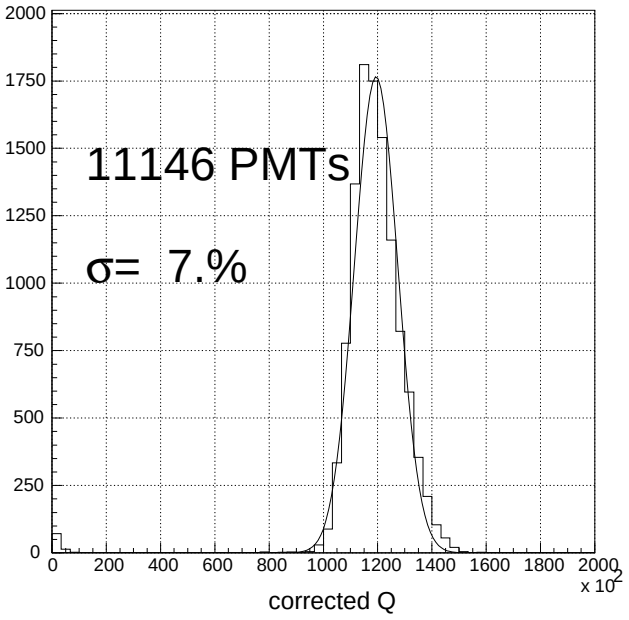

Figure 4.2: The gain variation for all PMTs after the high-voltage adjustment (x-axis shows corrected charge($\mathrm{pC} \cdot \mathrm{m}^2$))

Although the requirement for the absolute energy calibration is mono energy 5 $\sim$ 10MeV, such a γ-ray source is not available. Therefore, Ni source which emits several γ-rays 5 $\sim$ 10MeV is used to obtain 9MeV γ-ray at thermal neutron capture in Ni(n,γ)Ni*. Since the Super-Kamiokande detector has large volume, absolute energy scale may be strongly dependent on the detector position. The calibration using neutron capture with Ni could be carried out at several different position because Ni γ source system is compact and can be moved.

Also the detector can detect Cherenkov light from secondary electron by Compton scatter and electron pair creation. It is indirect measurement of electron energy. The direct measurement is described in next section.

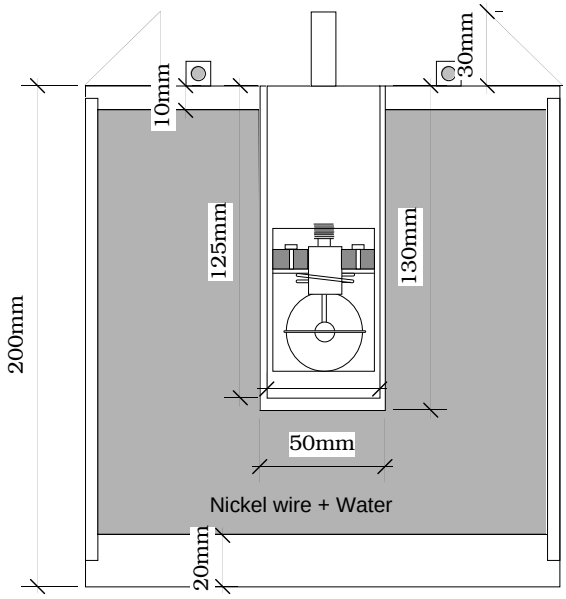

Figure 4.3: The schematic view of Ni calibration system

4.2.2 Calibration using electron linear accelerator

The calibration using electron linear accelerator(LINAC) is direct measurement of energy for single electron. The LINAC can generate the desired electron beam energy using collimators and magnets. The electron from LINAC is injected to the Super-Kamiokande detector. the electron energy is set planned energy between 5-20MeV.

The beam pipe is installed from top of the tank, The measurement can be done at variable position in inner-detector by changing the beam pipe length. The schematic view is shown in Fig.4.4.

The advantages using this calibration are direct energy calibration using electron, mono-energetic electron with $5 - 20$MeV energy electron. However, it is inconvenient for study of position and direction dependence. Because it is very large heavy system

compared with Ni calibration equipment, further LINAC can generate only under going electron.

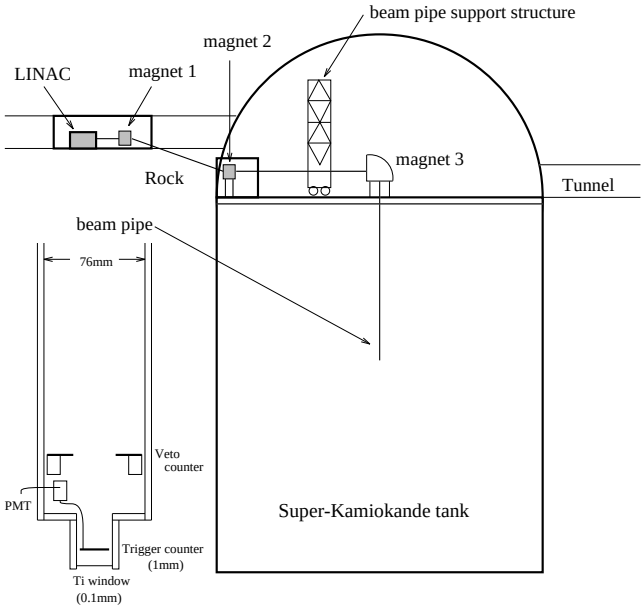

Figure 4.4: Configuration of LINAC calibration system

4.2.3 μ decay-e event method

The μ decay electron event method is useful source of the energy calibration for electrons around a few tens of MeV. The energy spectrum for μ decay electron is expressed as Eq.4.1.

$$\frac{dN}{dE_e} = \frac{G^2}{12\pi^3} m_\mu^2 E_e^2 \left(3 - \frac{4E_e}{m_\mu}\right) \tag{4.1}$$

where E_e is the energy of decay electron, G is the Fermi coupling constant, m_μ is the mass of muon. The maximum energy and mean one of muon decay electron is 53MeV and 37MeV, respectively.

The energy distribution of muon decay electron is shows in Fig.10.5, a solid line shows Monte-Carlo result and cross shows data. The difference in the low energy region is found. The reason of this difference is described in Section 10.3.2.

4.3 Timing calibration

Timing response of each PMT is not uniform. The differences come from fluctuation of transit time in each PMT and timing response of the discriminator. In order to calibrate

the difference of timing response, the transit time difference and pulse height dependence of the timing response are measured using the timing calibration system. Fig.4.5 shows the schematic view of the timing calibration system.

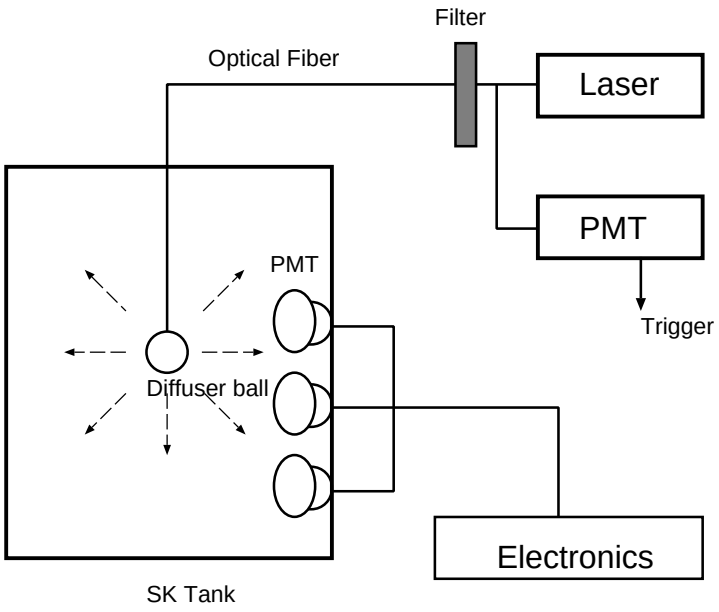

Figure 4.5: Schematic view of timing calibration system

The diffuser ball is located at the center of the tank. The distance from the position of each PMT to the diffuser ball is considered in TOF calibration.
Fig.4.6 is the T-Q maps which shows the relation between the mean value of the time and the charge from the PMT. The T-Q maps are made for each PMT and the measured time information is corrected using the T-Q maps. The timing resolution after correction by T-Q maps is shown in Fig.4.7 as 3nsec at one photo-electron.

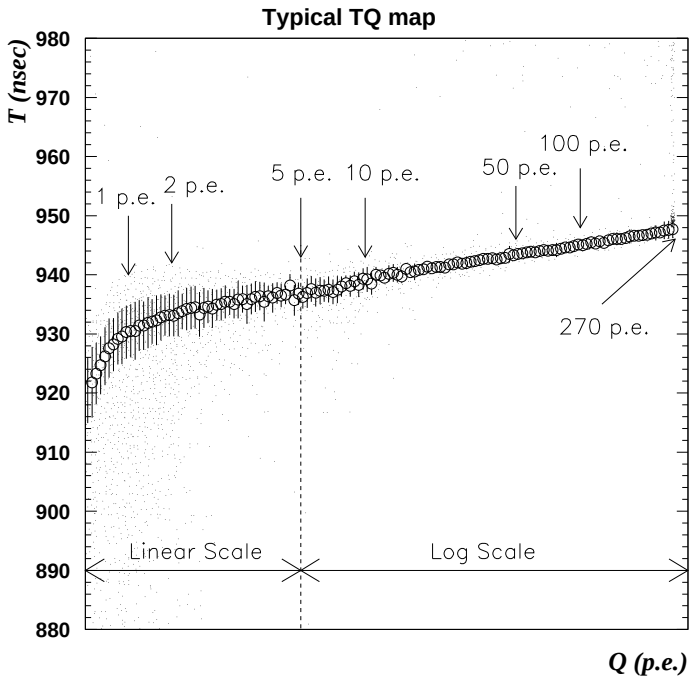

Figure 4.6: T-Q map of a typical PMT

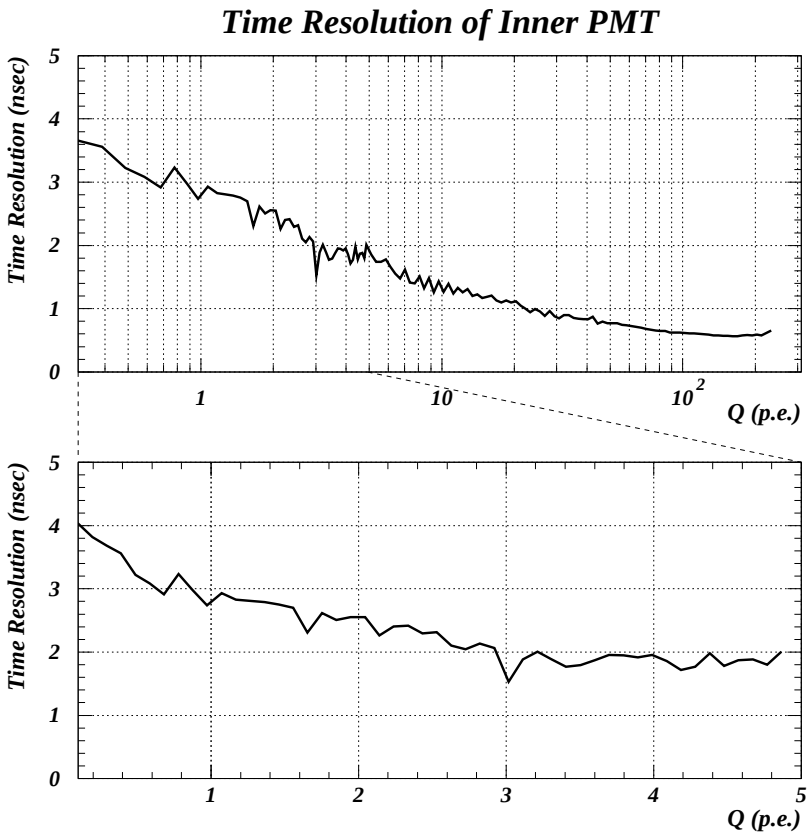

Figure 4.7: Timing resolution

4.4 Water transparency measurement

Since the transparency is about 60m, the water transparency determines the number of Cherenkov photons at the PMTs, and it affects to detector response. Then it is important to estimate the water transparency for data analysis.

Two kinds of transparency measurement are done in Super-Kamiokande, one is using cosmic-ray muon events, another is using the laser system.

4.4.1 Water transparency by cosmic-ray μ events

The cosmic-ray through-going muon from top to bottom into the tank is useful for monitoring the attenuation length. The entrance point and exit point is determined by automatic directional fitting.

The total charge(Q_i) detected by each PMT is described as the following equation(Fig. 4.8),

$$Q_i = const. \times \frac{f(\theta_i)}{l_i} \cdot e^{-\frac{l_i}{L}}$$

L	:	attenuation length
θ_i	:	the incident angle for Cherenkov light
$f(\theta_i)$	:	acceptance function of PMT
l_i	:	the flight length of Cherenkov photon

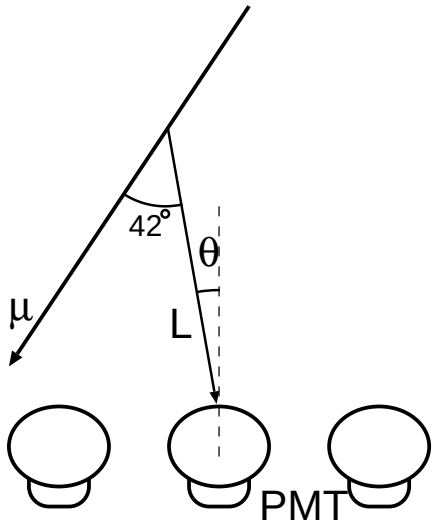

Figure 4.8: Schematic view of cosmic-ray muon method

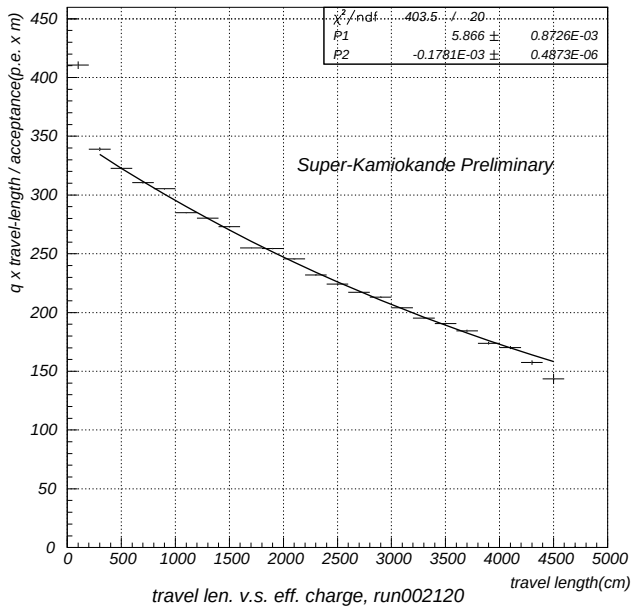

Figure 4.9: The light attenuation length(6th July 1996)

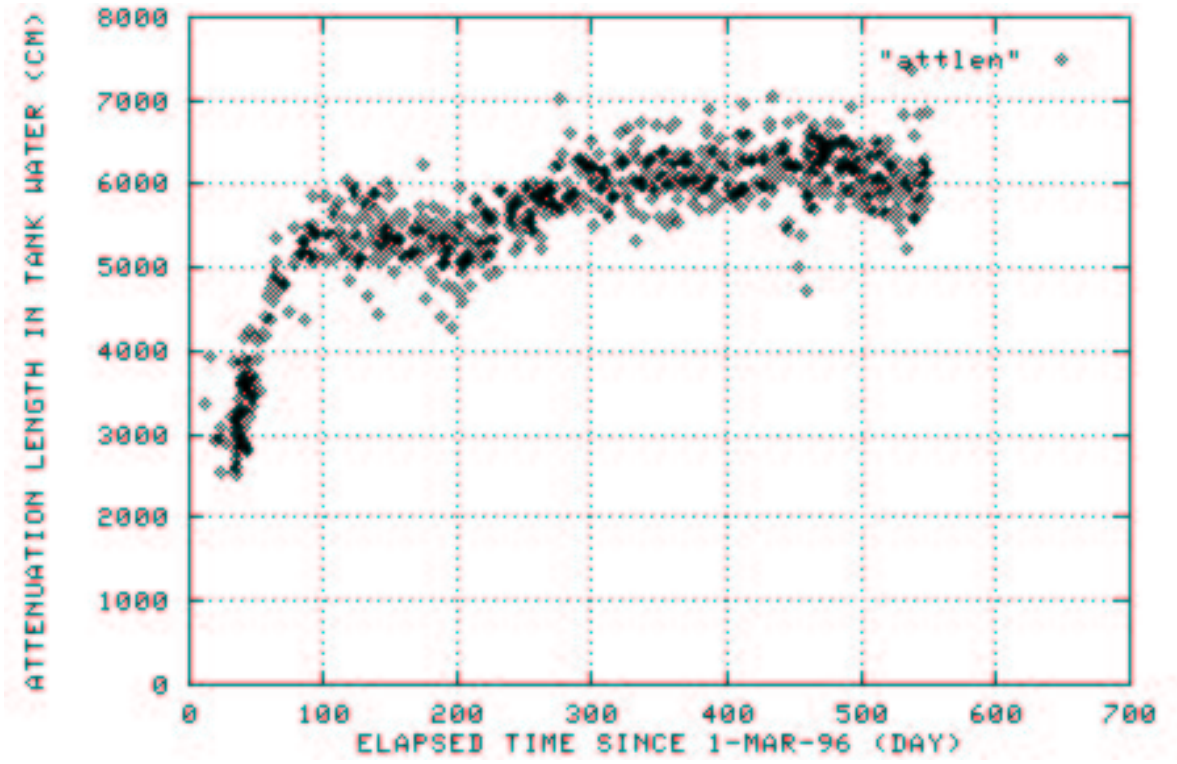

Figure 4.10: Time variation of the water attenuation length

Fig. 4.9 shows $\log\left(\frac{Q_i L}{f(\theta_i)}\right)$ plot against l in a typical run. The attenuation length was estimated to be 105.4 ± 0.5m(error of the fitting) in water from Fig. 4.9.

The attenuation length is estimated for each run. At the just starting this experiment, the attenuation length was around 60m. After the water purification system is running and makes very pure water, the attenuation length attained to be about 100m and be maintained stably.

4.4.2 Water transparency by laser

The directly measurement of water transparency is carried out by using the laser system which consists of the laser and CCD camera shown as in Fig. 4.11.

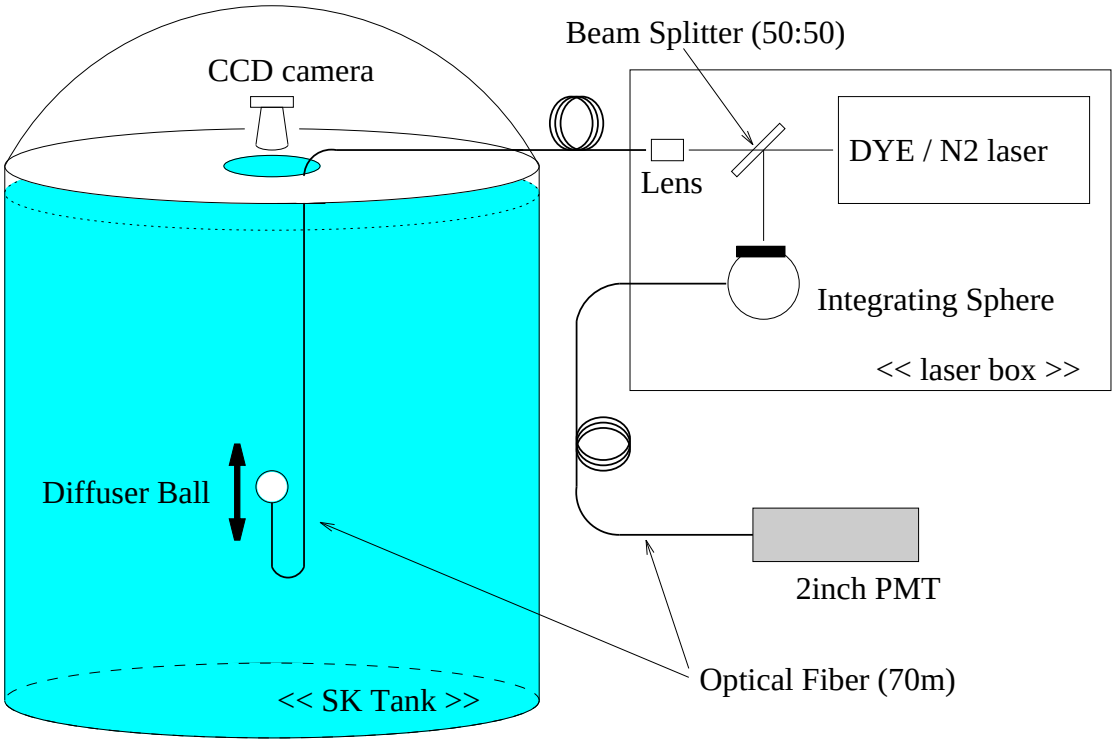

Figure 4.11: Set up of the laser system

The light source is a dye laser pumped by a pulsed N_2 laser. The emitted light divides into two optical fibers, the one is for monitoring PMT which measure the light intensity directly, the another is guided to the diffuser ball which is located in the water. The diffuser ball emits the isotropically light. The CCD camera measure the intensity of the attenuated light from diffuser ball. The depth of the diffuser ball is changed from 5m to 30m, I_{laser}(the light directly intensity at the laser) and I_{CCD}(the attenuated intensity at the CCD) are measured at each point. The attenuation length(L_λ) is expressed to be

following equation,

$$\frac{I_{CCD}}{I_{laser}} = const. \times exp\left(-\frac{l_d}{L(\lambda)}\right), \tag{4.2}$$

where λ is the wave length of the light. The experimental $\frac{I_{CCD}}{I_{laser}}$ is shown at the wave length of 400nm in Fig. 4.12. The data is fitted by Eqn. 4.2 and the attenuation length is obtained to be 92.2±5.2m.

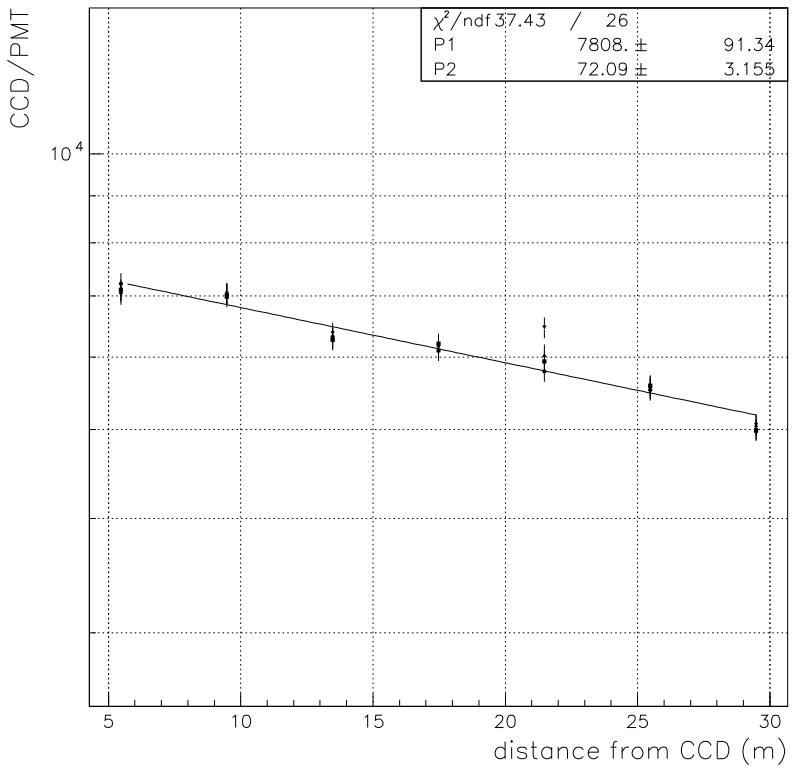

Figure 4.12: The attenuation length

Chapter 5

Data reduction

The trigger rate for all of Super-Kamiokande data is about 10Hz. But about 80% of the events are background which is are either low energy electron events or noise events. These background events are removed by automatically or manually. In this chapter, the event selection for upward-going muons is described.

5.1 Dataset

The Super-Kamiokande detector started in April 1996. The data earlier than July 1996 was not used for the analysis of stopping muons because the outer-detector was not stable before that time and the reduction for upward-going muons needs outer-detector information. Thus, the data from July 1996 to April 2000 for stopping muons and from April 1996 to April 2000 for through-going muons were studied. The live-time for stopping muons and through-going muons were 1247days, and 1268days, respectively.

5.2 Automatic reduction

The reduction flow chart is shown in Fig. 5.1. The first reduction, called 'online reduction', is a high speed and rough process. The second reduction, which is called 'offline reduction', required high precision and is a more precise process. In eye scan, physicists judge the event type and reconstruct the track of particle. I will describe these reduction processes.

5.2.1 Upward stopping muons

1st reduction

This reduction applied for rejection low energy γ-ray from radioactivity and through-going events.

- Total Q cut
  A large amount of background, about 80% of all events, are low energy events or

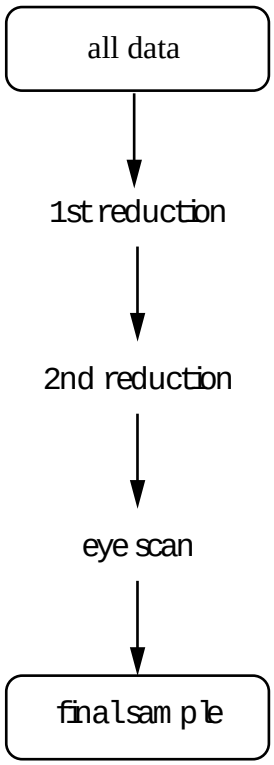

Figure 5.1: The flow chart of event selection.

γ-ray from radioactive sources present in the water or from outside of the detector. The first reduction applied a total Q cut for rejection these background. Events with less than 1000p.e. in total Q were rejected. Total Q means a summation of the charge from all PMTs for one event.

- Outer-detector cut
  Outer-detector cut is applied in order to reject through-going muons. The event rate due to muons in the Super-Kamiokande is about 2.2Hz. Muon events are categorized into through-going events and stopping events. The rate for stopping muon event is about 5% of all muon data.

  Through-going muon and stopping muon events are topologically defined by outer-detector information. Through-going muons go through the anti-detector with signals corresponding to entrance and exit points. Stopping muons stopped in the detector and a single signal is made in the anti-detector. Two kinds of cut are applied to reject through-going muons.

  - Cluster cut
    When charged particles go through the PMT layer of the inner-detector and the outer-detector, Cherenkov light forms some clusters of the active PMT. Stopping muon and through-going muon have different topological character

of the clusters. The topological difference is in the number of clusters produced in the outer-detector. In the through-going muon case, the muon generated outside of the outer-detector goes into and through out the outer-detector, two clusters appear in outer-detector, the entering cluster and the exit cluster. In the stopping muon case, only one cluster appears, the entering cluster. Therefore we need to know the number of clusters for each event to discriminate between through-going muons and stopping ones. At first, we select hit PMTs with the time between 500nsec and 1300nsec. Then the geometry of the selected PMTs and the number of these PMTs neighboring each other is estimated and defined as a cluster candidate. If the cluster candidate has more than 8 PMTs and the distance between them is less than 8m, then the candidate is judged as a cluster. The location of clusters is defined as the PMT position with maximum photo electrons. The events which have two clusters are removed from the stopping muon data and kept as through going muons.

- Time-window cut
  The other method for the separation of stopping and through-going muons is a time-window cut which uses the difference of time width for PMT hits. Stopping and through-going muons differ in the time of flight for muon in the outer-detector. The time width for the through-going muon is larger than the stopping one. The time width is determined as follows. At first, the number of hit PMTs is counted in the time-window between 800nsec and 900nsec. Next, the time-window is moved by 1nsec, that is between 801nsec and 901nsec, and the number of hit PMTs is again counted. This counting of PMTs and moving of the time-window is repeated 500times. The time width is determined as the number of 100nsec time-windows where there are more than 15 hit PMTs. An event whose time width is longer than 240 nsec is judged to be through-going muons and is removed.

- Detection efficiency
  The reduction factor for through-going muons is estimated by using the cosmic-ray muon data applied with total Q cut. The reduction factor of through-going muons by outer-detector cut is 96%. However, 76% of through-going muons which could not be eliminated are events with a shorter track length than 5m ($E_\mu \sim 1.2$GeV) in the inner-detector. The detection efficiency for stopping muon is estimated to be 98.6% by time-window cut and 99.9% by cluster cut using cosmic-ray event. Therefore the combined detection efficiency for stopping muons after all anti-detector cuts is 98.5%. Moreover, an estimation of the detection efficiency for stopping muon is carried out using Monte-Carlo(MC) data, with neutrino induced muons at higher energy than 1.6GeV for muon energy. The detection efficiency for stopping muons by outer-detector cut for MC event is obtained to be 95.9%.

Because neutrino induced upward stopping muons could interact with the water of the anti-detector, the efficiency obtained by using upward stopping muons could be different with the efficiency obtained by using cosmic-ray muons. Therefore, the detection efficiency for muons was adopted 95.9% using MC data. The discrepancy between the MC result with and the cosmic-ray result is included as systematic error.

2nd reduction

- Total Q cut
  Total Q(charge) cut for the 2nd reduction is applied to reject short track length events.

  Fig. 5.2 shows the relation of total Q with track length by manual reconstruction for cosmic-ray stopping muons. Since a short track length event is difficult to reconstruct, events in which its orbit has longer than 7m of track length are collected. The 7m track length is equivalent to 1.6GeV in energy for a muon.

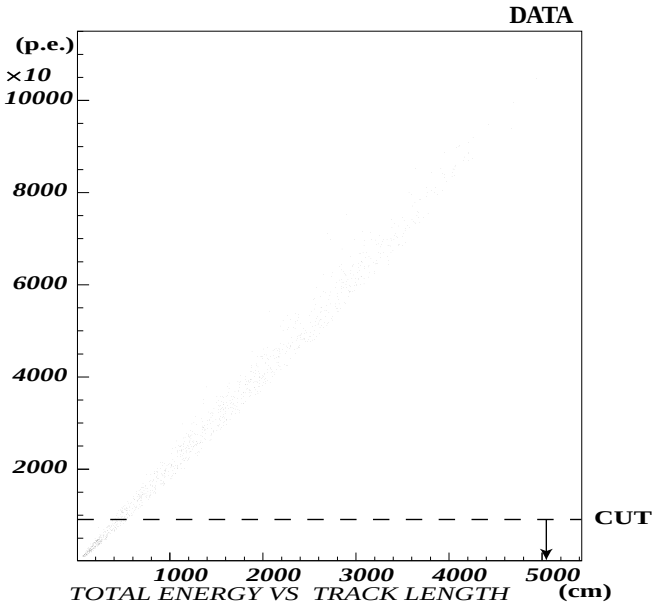

Figure 5.2: Total photo-electron and track length for stopping muons. Stopping muons collected by eye scan were fitted by hand and were determined their track length.

- μ direction cut
  Stopping muons are grouped as either cosmic-ray induced or atmospheric neutrino induced muons. Since cosmic-ray muons are almost downward-going and upward going muons are almost neutrino induced, downward-going muons are rejected as background event. The direction of muons is obtained by directional reconstruction(stopping muon fit). The horizontal downward events with $\cos\Theta_z < 0.12$ are

collected to estimate for contamination of cosmic-ray muons, where Θ_z is zenith angle; $\cos\Theta_z = -1$ is defined as vertically upward. The obtained contamination of the cosmic-ray muons are in $\cos\Theta_z < 0.12$.

The method of automatic directional reconstruction is as follows,

- Determination of entrance point
  Since the particle coming from the outer-detector and going into the inner-detector makes entrance cluster at first, the PMTs at the entrance point get hit earlier than other one. However, some noise events could happen in similar timing sequence, for example dark noise of PMTs. Therefore, the position of the earliest hit PMT whose neighbor PMTs get hit within 5nsec is taken to be the entrance point.
- Directional reconstruction for muons
  The direction at the entering point on the inner-detector wall is determined by using a grid search method. At first, muon direction is approximated from the muon entering point to the center of Cherenkov ring which is determined by a center of mass in charge produced in PMTs. The grid search is carried out by changing the virtual direction starting from the initial direction and by minimizing the fitting evaluation function. The fitting function 'goodness' is as follows,

$$goodness = \frac{1}{\Sigma\frac{1}{\sigma_i^2}} \times \Sigma\frac{1}{\sigma_i^2} exp\left[-\frac{1}{2}\left(\frac{t_i - T_i}{1.5\sigma_i}\right)^2\right] \tag{5.1}$$

  where t_i is the hitting time for each PMT, σ_i is the timing resolution(=3nsec), and T_i is the hit time of each PMT estimated from T, the entering time of muon. T_i is calculated as follows,

$$T_i = T + \frac{l_\mu}{c} + \frac{n \cdot l_{ph}}{c} \tag{5.2}$$

  where c,n are light velocity in vacuum, and the refractive index of water($n = 1.344$), respectively. l_μ is the distance from the entering point to the Cherenkov emission point along the muon track. l_{ph} is the distance from the Cherenkov emission point to each PMT(Fig.5.3). Since the fitting result agrees with the data, when goodness is closest to 1, it means completion of the fitting and grid search. Thus, entrance point and direction are obtained.

- Detection efficiency
  The 2nd reduction was applied to upward stopping muons generated by MC detector simulation. The detection efficiency was 100% in all direction. Subsequently, the 2nd reduction was applied to cosmic-ray muons. The result is shown in the table 6.1. The detection efficiency for cosmic-ray stopping muons is almost 100% in all directions.

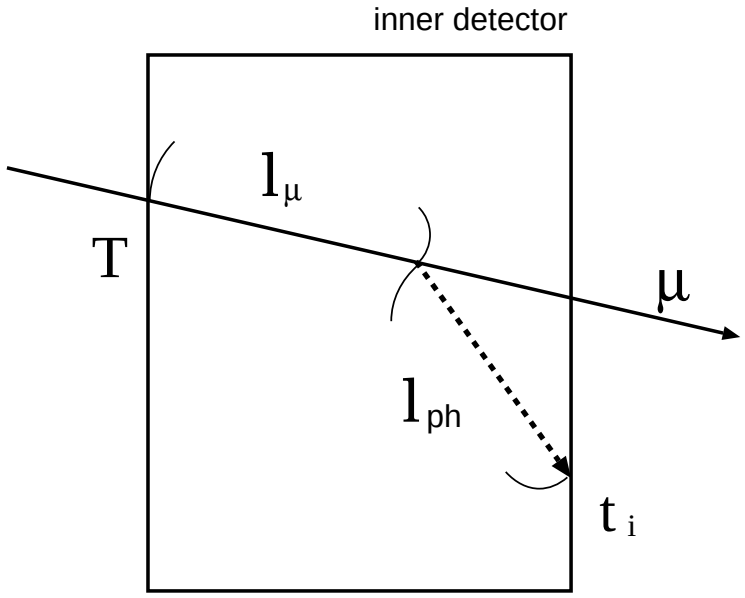

Figure 5.3: Schematic view of TOF.

5.2.2 Upward through-going muons

1st reduction

- Total Q cut
  Both low energy and noise events are eliminated with a cut on total Q $\leq$ 5000p.e. same as stopping muon reduction.

- Maximum Q cut
  The charge of PMTs at exit point must be largest charge because of the no attenuation of photons. Single-ring stopping muons, which has no exit point, are rejected by this selection. Events having maximum Q larger than 235p.e. are chosen as through-going events.

- The position dependence of the maximum Q PMT cut
  In the through-going muon case, the position of the PMT with maximum Q must be close to exit point. Therefore, the distance between entrance point and maximum Q PMTs position(L_{ent}) is large. On the other hand, the distance between exit point and maximum Q PMTs position(L_{ext}) is small. The entrance and exit point is estimated by using same process as stopping muon reduction process. The selection $L_{ent} \geq$ 300cm and $L_{ext} \leq$ 300cm are applied. The event with $L_{ent} \leq$ 300cm is judged as stopping muons. The event with $L_{ext} \geq$ 300cm is classified into the multiple muon event. Therefore, these two kinds of events were rejected.

- μ direction cut

The down-going cosmic-ray muons are eliminated by using same reduction routine as stopping muons selection. The event with larger goodness than 0.88 is chosen as the good event. All fitted events are selected by zenith angle with $\cos\theta \leq 0.1$

2nd reduction

- Total Q cut
  The total Q cut is applied on the events through first reduction in order to make the performance of the track length reconstruction better. The events with less than 12000p.e. in total Q, corresponding to 5m in track length, were rejected. The total Q cut and maximum Q cut are shown in Fig 5.4.

- μ direction cut
  In the 2nd reduction, two kinds of the directional fit are applied. These are more precise processes than 1st reductions one. One is based on time-of-flight and other is based on charge of PMTs.

  The following function is defined for the time-of-flight based reduction,

$$TOF - \sigma = RMS(T_i - TOF_i) \tag{5.3}$$

$$TOF_i = \frac{l^i_\mu}{c} + \frac{n l^i_{ph}}{c} \tag{5.4}$$

  where i is the index of a PMT number, T_i is the timing information of i-th PMT. l_μ and l_{ph} is described in stopping muons reduction. Fig 5.3 shows the definition of l_μ and l_{ph}. A smaller $TOF - \sigma$ means a better muon fitting.

  Another function is R_{cone}, based on charge information. R_{cone} means the ratio of hit PMT numbers and is defined as follows,

$$R_{\mathrm{cone}} = 1 - \frac{N_{\mathrm{hit42}}}{N_{\mathrm{PMT42}}} + \frac{N_{\mathrm{hit70}}}{N_{\mathrm{PMT70}}} \tag{5.5}$$

  where N_{hiit42} and N_{PMT42} are the number of hit PMTs and the number of PMTs in 42° Cherenkov cone, respectively. N_{hit70} and N_{PMT70} are the number of hit PMTs and the number of PMTs between 70° cone and 42° cone. The defined threshold of the hit PMT is $\sqrt{\text{total Q}/100}$. In equation 5.5, the second term N_{hit42}/N_{PMT42} shows the filledness of the Cherenkov ring and third term N_{hit70}/N_{PMT70} shows the sharpness of the edge of the Cherenkov ring. Therefore, if the event is through-going muon, N_{hit42}/N_{PMT42} shows a larger value and N_{hit70}/N_{PMT70} shows a smaller value. Then, a smaller R_{cone} means a better muon fitting.

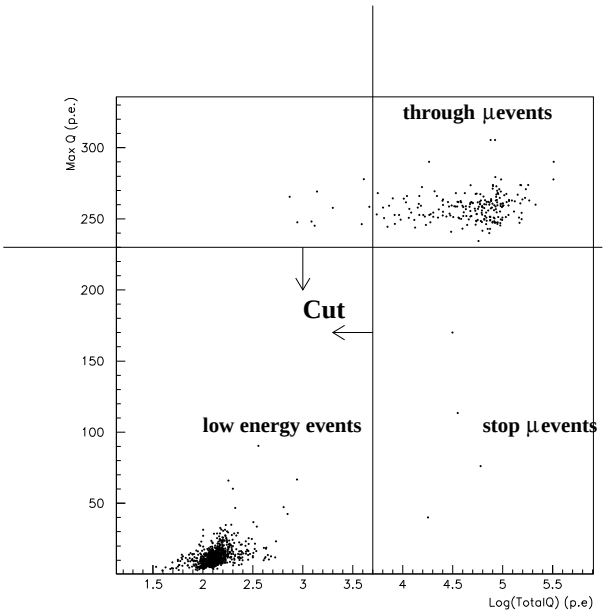

Figure 5.4: Total Q cut and maximum Q cut

5.3 Eye scan with manual fitting

The elimination of short track length events is difficult by means of the automatic directional reconstruction. After the second reduction, edge clipping events still remain which go through or along the edge of the inner-detector wall. However, edge clipping events are categorized as through-going muon in the reduction process. At the second reduction, because the number of clusters is only one at the edge of the detector, they were placed into the same category as stopping muons. Therefore, the eye scan by physicists was applied to all events remaining after automatic reduction. As mentioned already, the stopping muons are categorized the events with only one cluster and more than 7m track length in the inner-detector.

The directional resolution for muons becomes better by means of manual reconstruction by physicists. The manual reconstruction is performed by selection of the entrance and the exit points, the exit point is determined by extrapolation from entrance to stopping direction. The resolution for directional reconstruction manually is estimated to be 1.4° using MC events, (Fig. 5.5). Also individual human bias is obtained to be 0.8°(Fig. 5.6) from angular difference comparing the results of two independent scanners. The contamination of through-going muons with stopping muons is estimated to be lower than 1%. Since the eye scan was applied by two independent groups, the eye scan reduction could be accomplished with almost 100% efficiency.

5.3.1 Track length cut

Since the directional reconstruction is difficult for short track length events and the background other than muons should be taken into account in the low energy region, events with longer than 7m track length(equivalent to 1.6GeV in muon energy) were adopted for final data.

The track length of through-going muons is geometrically determined from the entrance and exit points. However, for stopping muons, track length should be estimate from particle energy at entrance. Algorism of the track length calculation is described below. Coarse direction and entrance point are obtained by manual reconstruction. Next, cone with opening angle of 70° cone is put on the entrance point in order to obtain rough total charge. The charge of all PMTs inside the approximated 70° cone is summed as the total charge. The charge is applied some collections, water transparency and acceptance by PMT geometry. The momentum is estimated from the total charge and the track length is calculated from the momentum by using the muon energy loss of Lohmann's calculation.

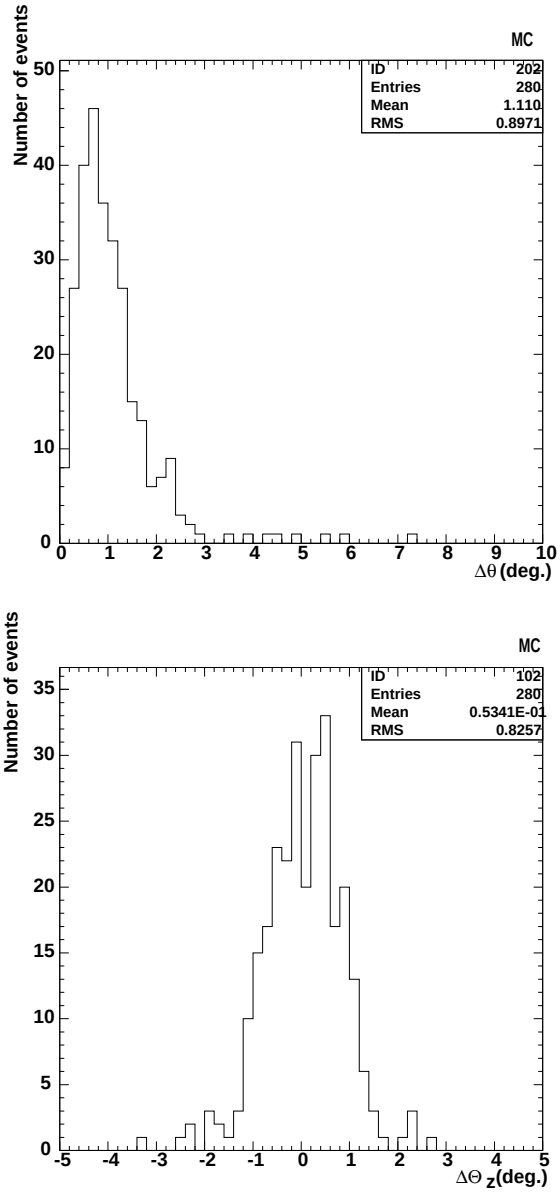

Figure 5.5: Angular resolution for MC stopping muons $\mu(E_\mu > 1.6GeV)$. Upper figure is angle between manual reconstruction and true direction. lower one is zenith angle view$(\Theta_{gen} - \Theta_{ma})$.

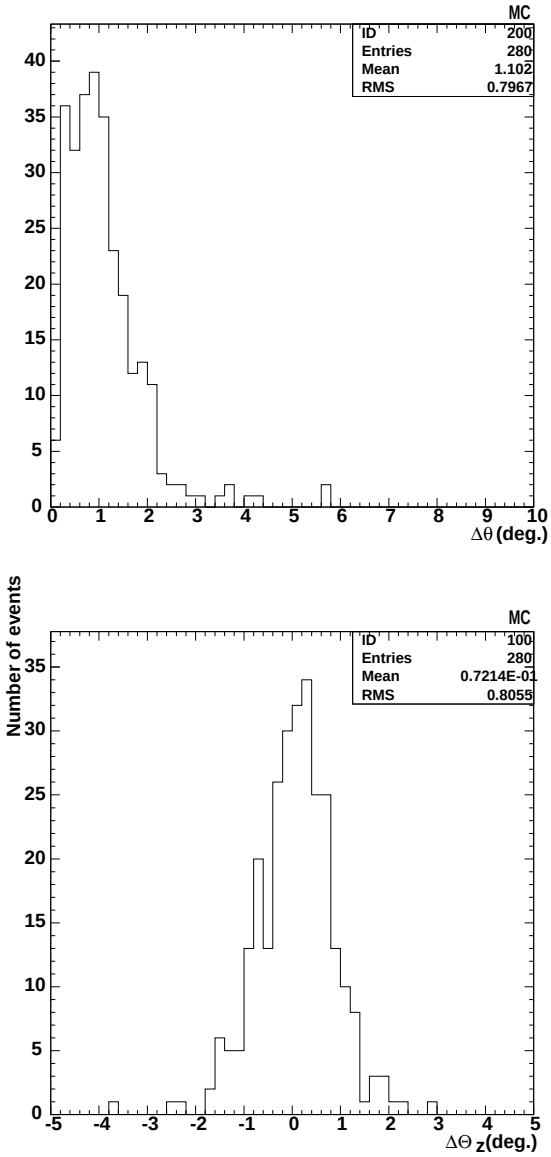

Figure 5.6: Angular difference depend on the scanner, upper figure is angular difference by two scanner. Lower figure is zenith angle view.

5.4 Upward-going muon events

After all event selection, The final data is selected. The scatter plot of the vertical angle versus azimuth angle distribution of the final data is shown in Fig. 5.7. Cosmic-ray contamination is clearly seen in thin rock region between $\phi = 120°$ and $\phi = 180°$. Finally, 143 events were observed as upward stopping muons.

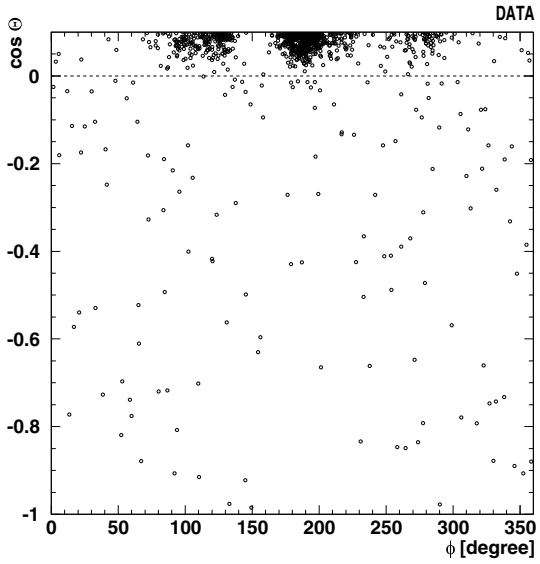

Figure 5.7: Zenith angle and azimuth angle for stopping muons.

5.5 Backgrounds

We considered the reason of background for upward stopping muons.

1. Cosmic-ray muons contamination
   The horizontal downward cosmic-ray muons are possibly mistaken as upward-going muons due to finite resolution of directional manual reconstruction. In Fig. 5.7, regions with higher density of points, possibly due to this background, are seen in the region vertical angle $\cos\Theta \approx 0$(near horizontal) and azimuth angle between $\phi = 120°, \phi = 180°$. Since cosmic-ray contamination depends on the amount of rock surrounding the detector and the shape of Ikenoyama mountain, cosmic-ray down-going muons penetrate from relatively thin rock direction. In Fig. 5.9, region (2) is thin rock direction, the thin rock region is defined as the region that the azimuth angle between 60° and 310°, and the zenith angle smaller than -0.1 of cosine. Region (1) is outside of the region (2). Fig. 5.8 is plotted two region defined as the region (1) and (2) in Fig. 5.9 in zenith angle distribution separately, (1) and

(2) region, are normalized in shown azimuth angle respectively. The horizontal line in center of figure is shown border between downward and upward. Although both distribution is flat in upward region $\cos\Theta < 0$, the number of muons is increasing exponentially with $\cos\Theta$ in due to downward-going in the region (2) cosmic-ray muons.

The number of cosmic-ray contamination into upward region is estimated by extrapolation the distribution of (2) and fitting of exponential function and integrate the exponential slope in the upward going range as follows,

$$\text{Number of contamination} = \int_{-1}^{0} e^{(a+b)} d\cos\Theta \tag{5.6}$$

The number of cosmic-ray muons contamination is estimated to be 22 ± 10 events for upward stopping muons and 10 ± 0.9 events for upward through-going muons.

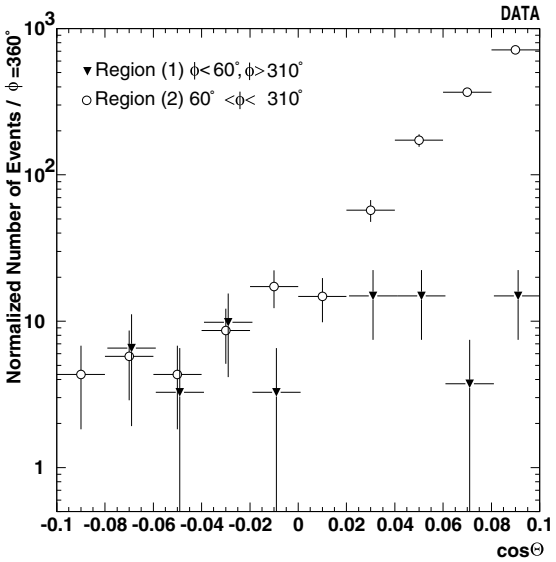

Figure 5.8: Zenith angle distribution of stopping muons. The region (1) is thin rock direction, the region (2) is thick rock direction in azimuth angle. Cosmic-ray contaminations are seen apparently in thin rock region.

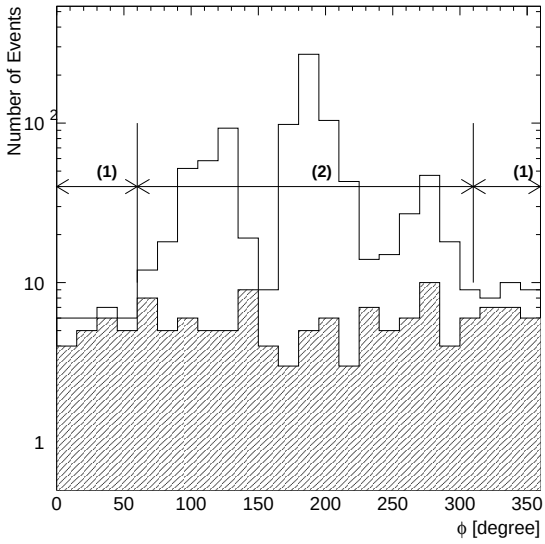

Figure 5.9: The azimuth angle distribution for stopping muons. The region (1) is thick rock direction, the region (2) is thin rock direction. Three peaks due to contamination downward-going cosmic-ray are seen in thin rock region.

Chapter 6

Observed flux

The experimental upward-going muons flux(Φ_{obs}) is calculated by using live time(T_{live}), effective area of the detector(S), and selection efficiency(ϵ). The upward-going muons flux is expressed by the formula,

$$\Phi_{obs} = \frac{1}{2\pi T_{live}} \times \sum_{j=1}^{N} \frac{1}{\epsilon(\theta_j) S(\theta_j)} \tag{6.1}$$

where θ_j is the zenith angle of the j-th upward going muon, 2π is the total solid angle covered by the detector for upward-going muons, and N is the total number of observed upward-going muon events. Fluxes of observed upward stopping muons and through-going muons are estimated from equation 6.1.

6.1 Live time

The detector live time is calculated by following equation,

$$T_{live} = T_{run} - T_{pedestal} - T_{dead} \tag{6.2}$$

where T_{live} is the detector live time, T_{run} is the pedestal event time, T_{dead} is the detector dead time. The detector dead time means all or a part of event information is lost by electrical or network trouble. The total detector live time is estimated to be 1247days for upward stopping muons, and 1268days for upward through-going muons. The difference appeared for the detector live time of upward stopping muons and through-going because the instability of the detector deteriorates more intensively the events with stopping muons. The live time is about 90% of the true time.

6.2 Effective area

The effective area is the required area in order to get enough information for upward-going muons which have a given direction, the sensitivity depends on the azimuth angle and the

zenith angle of the path of the muons. In this analysis upward-going muons with longer than 7m track-length are required. But a non sensitive region is available because of the cylindrical detector. The area which have longer than 7m track length in the detector is called the effective area.

The effective area is calculated as follows and the schematic view is shown in Fig 6.1. A large enough plane, having two-dimensional grid points with every 10cm step, is defined out of the detector. A vertical line on the defined plane is drawn from each grid point to the detector. If the length of line crossing the detector is longer than 7m, the corresponding grid point is counted for a part of the effective area. Finally the effective area is calculated for every zenith angle of the area divided into 100 directions. The result of the effective area calculation is shown in Fig. 6.2.

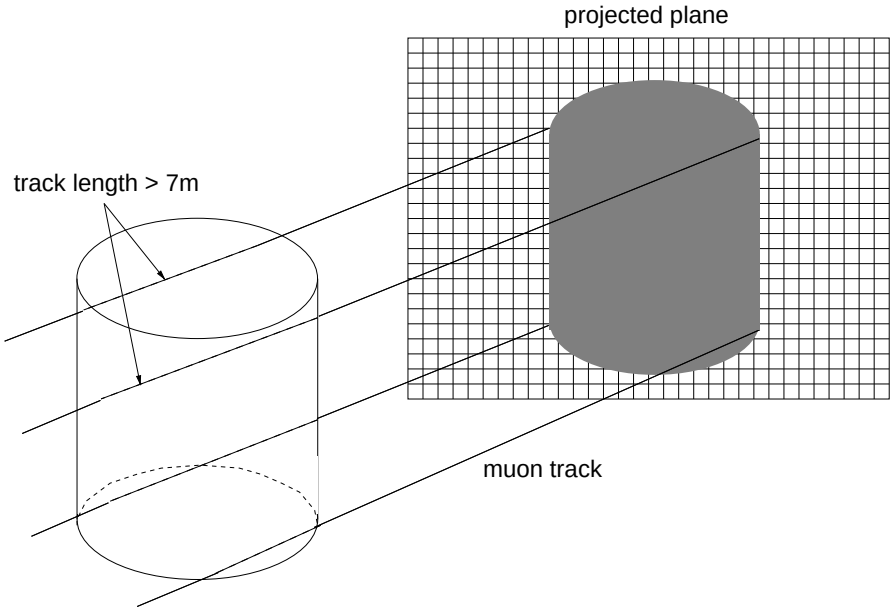

Figure 6.1: Schematic view of effective area.

6.3 Selection efficiency

The selection efficiency is the detection probability for the upward-going muons estimated for each zenith angle bin, with the range $-1 \leq \cos\theta \leq 0$ being divided into 10 bins. The selection efficiency depends on 1st and 2nd reduction efficiency because the selection efficiency for eye scan is almost 100%. The result for selection efficiency is shown in table 6.1

The selection efficiency for the most horizontal bin is slightly smaller than any other bin because of the resolution of automatic fitters. It is possible that true upward-muons

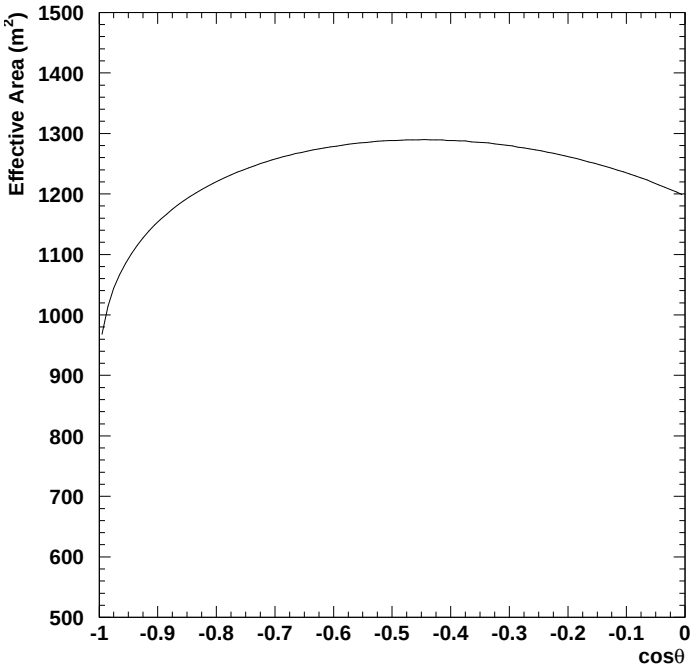

Figure 6.2: Zenith angle dependence of the effective area.

cosθ	-0.95	-0.85	-0.75	-0.65	-0.55	-0.45	-0.35	-0.25	-0 .15	-0.05
stop	1.00	1.00	1.00	1.00	1.00	1.00	1.00	1.00	0.99	0 .98
thru	1.00	1.00	1.00	1.00	1.00	1.00	1.00	1.00	1.00	0 .99

Table 6.1: The summary for selection efficiency.

could be judged as downward-going muons.

6.4 Systematic errors

The systematic errors are categorized into two cases: one which depends on the event category(whether stopping or through-going), the other is independent of event category. The independent errors are live time and effective area, while the dependent errors are track length and reconstruction efficiency. The uncertainty for cosmic-ray contamination, which has been described in Section 5.5 and was estimated from down-going muons($0 \leq \cos\theta \leq 0.1$), is included in the statistical error.

Track length

The reconstructed track length for upward stopping muons is described in Section 5.3.1. The difference of the track length between reconstructed from total charge of cosmic-ray stopping muons and calculated from entering point to stopping point with MC is 5%. When the track length cut with 7m is changed $\pm 5\%$, the upward stopping muon flux is changed $+4.9\% - 4.1\%$. The systematic error of track length for upward through-going muons is determined to be 1% by geometric uncertainty for the Super-Kamiokande detector.

Reconstruction efficiency

The reconstruction efficiency for upward stopping muons is described as section 5.2.1, the difference of the efficiency between cosmic-ray muons and MC is 2.6%, and corresponds to 1% for upward stopping muon flux. For the upward through-going muons, the reconstruction efficiency is near 100% as shown in table 6.1. Thus the systematic error is negligible.

Systematic errors for observed flux

Table 6.2 shows the summary of systematic errors for observed upward-going muon flux. The systematic error for observed upward-going muon flux and through-going muon flux are estimated to be +5.2%-4.5%, and $\pm 1.2\%$, respectively.

6.5 Observed flux of upward going muons

In the 1247 live days for upward stopping muons, the observed flux is estimated to be $\{0.41 \pm 0.02(\text{stat.}) \pm 0.02(\text{syst.})\} \times 10^{-13} \text{cm}^{-2}\text{s}^{-1}\text{sr}^{-1}$. On the other hand, in 1268 live days for upward through-going muons, the observed flux is estimated to be $\{1.70 \pm 0.05(\text{stat.}) \pm$

(upward stopping muon flux)

track length	$+4.9\% - 4.1\%$
live time	$\pm 1\%$
reduction efficiency	$\pm 1\%$
total	+5.2% -4.5%

(upward through-going muon flux)

track length	$\pm 0.5\%$
effective area	$\pm 0.3\%$
live time	$\pm 1\%$
total	$\pm 1.2\%$

Table 6.2: The summary of systematic error for upward going-muons

$0.02(\text{syst.})\} \times 10^{-13}\text{cm}^{-2}\text{s}^{-1}\text{sr}^{-1}$. The total upward going muon flux which is a summation of stopping muon flux and through-going muons is $\{2.11 \pm 0.05(\text{stat.}) \pm 0.03(\text{syst.})\} \times 10^{-13}\text{cm}^{-2}\text{s}^{-1}\text{sr}^{-1}$, which is independent of the detector shape. The energy dependence of upward-going muon is estimated from the ratio of stopping muons to through-going muons flux, the ratio for stopping muon flux and through-going is $0.24 \pm 0.02(\text{stat.}) \pm 0.01(\text{syst.})$.

Chapter 7

Expected flux

The expected flux for upward-going muons are estimated for neutrino oscillation analysis. Neutrino oscillation is deduced by comparison between the observed flux and the expected one. The expected flux is usually estimated by Monte Carlo approach, but it is difficult in the upward-going muon case. Since a large amount of neutrino-nucleon interaction near the detector should be considered, the statistics are not enough for oscillation analysis. Therefore an analytical method to calculate the expected upward-going muon flux is adopted.
We give a detailed description of the analytical method to calculate the upward-going muon flux.

7.1 Analytical method

The atmospheric neutrino induced upward-going muon flux are calculated by using the atmospheric neutrino flux(Φ), the charged current cross section for the neutrino-nucleon interaction in the rock(σ_ν), and the muon range in the rock. The muon neutrino induced upward-going muon flux is expressed as follows,

$$\frac{d^2\sigma_\nu}{dxdy} \cdot \frac{d^2\Phi_\nu(E_\nu, \cos\theta_\nu)}{dE_\nu d\Omega} \tag{7.1}$$

where E_ν is the energy of atmospheric neutrino, x, y are Bjorken scaling parameters. The probability that the muon with energy E_μ produced by the neutrino-nucleon interaction goes through with $X(\mathrm{g/cm^3})$ in the rock and come into the detector is expressed with $g(X, E_\mu, \cos\theta_\nu)$. The upward-going muon flux with zenith angle θ_μ is calculated as follows,

$$\frac{d\phi_\mu(E_{th}, \cos\theta_\mu)}{d\Omega} = \int_0^\infty N_A dX \int_{E_\mu}^\infty dE_\nu \int_0^1 dy \int_0^1 dx \cdot \frac{d^2\sigma_\nu}{dxdy} \cdot \frac{d^2\phi_\nu(E_\nu, \cos\theta_\nu)}{dE_\nu d\Omega} \cdot g(X, E_\mu, E_{th}) \tag{7.2}$$

where N_A is the Avogadro constant. The θ_ν is nearly equal to θ_μ. Therefore θ_ν is taken to be θ_μ. The traveling distance is $R(E_\mu, E_{th})$, over which the muon loses energy from E_μ to E_{th} in traveling R. The function $g(X, E_\mu, E_{th})$ is,

$$g(X, E_\mu, E_{th}) = \Theta(R(E_\mu, E_{th}) - X) \tag{7.3}$$

where Θ is defined as,

$$\Theta(x) = \begin{cases} 1 & : \quad x \geq 0 \\ 0 & : \quad x < 0 \end{cases} \tag{7.4}$$

$$\int_0^\infty g(X, E_\mu, E_{th}) dX = R(E_\mu, E_{th}) \tag{7.5}$$

The equation (7.2) is rewritten as,

$$\begin{aligned} \frac{d\phi_\mu(E_{th}, \cos\theta)}{d\Omega} &= N_A \int_{E_\mu}^\infty dE_\nu \int_0^1 dy \int_0^1 dx \cdot \frac{d^2\sigma_\nu}{dxdy} \cdot \frac{d^2\phi_\nu(E_\nu, \cos\theta)}{dE_\nu d\Omega} \cdot R(E_\mu, E_{th}) & (7.6) \\ &= \int_{E_\mu}^\infty \left[\int_0^1 \left[\int_0^1 \frac{d^2\sigma_\nu}{dxdy} \right] N_A R(E_\mu, E_{th}) dy \right] \frac{d^2\phi_\nu(E_\nu, \cos\theta)}{dE_\nu d\Omega} dE_\nu & (7.7) \\ &= \int_{E_\mu}^\infty P(E_\nu, E_{th}) \frac{d^2\phi_\nu(E_\nu, \cos\theta)}{dE_\nu d\Omega} dE_\nu & (7.8) \\ & & (7.9) \end{aligned}$$

where the function P is defined as,

$$P(E_\nu, E_{th}) \equiv \int_0^1 \left[\int_0^1 \frac{d^2\sigma_\nu}{dxdy} \right] N_A R(E_\mu, E_{th}) dy \tag{7.10}$$

The function P is the probability that an neutrino with energy E_ν produces muons by neutrino interaction and the muons reach the detector with energy larger than E_{th}. Since the Super-Kamiokande detector can not discriminate between negative muons from muon neutrinos and positive muons from anti muon neutrinos, the total upward-going muon flux is estimated.

7.2 Atmospheric neutrino flux

The energy spectrum of atmospheric neutrino is calculated on the basis of the energy spectrum of primary cosmic-ray. The calculation of atmospheric neutrino flux needs the information about the composition of primary cosmic-ray and hadron interaction. Several models for the atmospheric neutrino flux are available. Energy spectra for atmospheric neutrino fluxes by Bartol[13], Volkova[14], Honda[15], and Butkevitch[16] are shown in Fig.7.1. The zenith angle distribution for various neutrino energy is shown in Fig.7.2

The upward-going muon flux at vertical upward ($\cos\theta = -1$) is larger than the one at horizontal($\cos\theta = 0$). The shape of the zenith angle distribution depends on the neutrino energy. The shape in low energy is flat while it is steep in high energy.

7.3 Neutrino-nucleon interaction

The atmospheric neutrino interacts with nucleon in the rock and produces muons. The cross section for charged current(CC) interaction is described in the following. The total

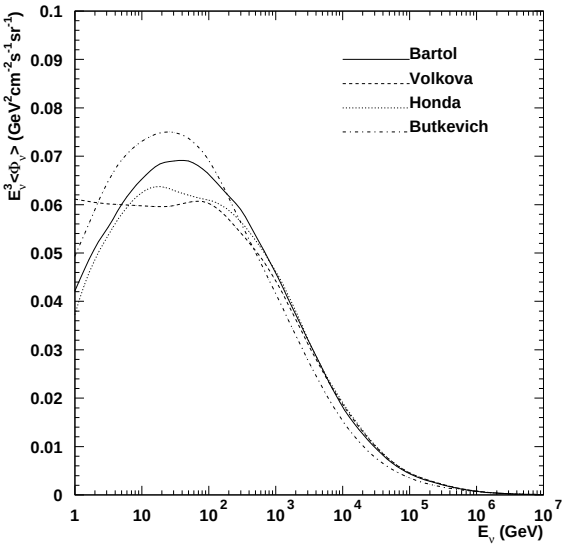

Figure 7.1: The energy spectrum of atmospheric neutrino($\nu_\mu + \bar{\nu}_\mu$) flux

cross section for charged current interaction of neutrinos is composed of deep inelastic scattering(DIS), quasi-elastic scattering(QEL) and single-pion production(1π).

$$\sigma^{CC} = \sigma^{DIS} + \sigma^{QEL} + \sigma^{1\pi} \tag{7.11}$$

The cross section for DIS is calculated on the basis of parton distribution function(PDF) which shows quark distribution in nucleus. The QEL and single pion production are also taken into consideration.

7.3.1 Deep inelastic scattering

The differential cross section when neutrino with E_ν produces muons with E_μ by charged current interaction is expressed by Bjorken scaling parameter($x = Q^2/2m_N E_\nu y$, $y = 1 - E_\mu/E_\nu$) is shown as follows,

$$\frac{d^2\sigma_\nu}{dxdy} = \frac{G_F^2 m_N E_\nu}{\pi} \frac{m_W^4}{(m_W^2 + Q^2)^2} \left[y^2 x F_1 + \left(1 - y - \frac{m_N x y}{2E_\nu}\right) F_2 \pm \left(y - \frac{y^2}{2}\right) x F_3 \right] \tag{7.12}$$

where the positive and negative signs in the last term correspond to ν and $\bar{\nu}$, respectively, G_F is the Fermi constant, m_W the mass of W boson, Q the momentum transfer between neutrino and muon. F_1, F_2, F_3 are the structure functions given by quark distribution functions $f_i (i =$ the flavor of quark) as follows,

$\nu_\mu n(p) \rightarrow \mu^- X$

$$F_2 \;=\; 2xF_1 = 2x[f_d(f_u) + f_s + f_b + f_{\bar{u}}(f_{\bar{d}}) + f_{\bar{c}} + f_{\bar{t}}] \tag{7.13}$$

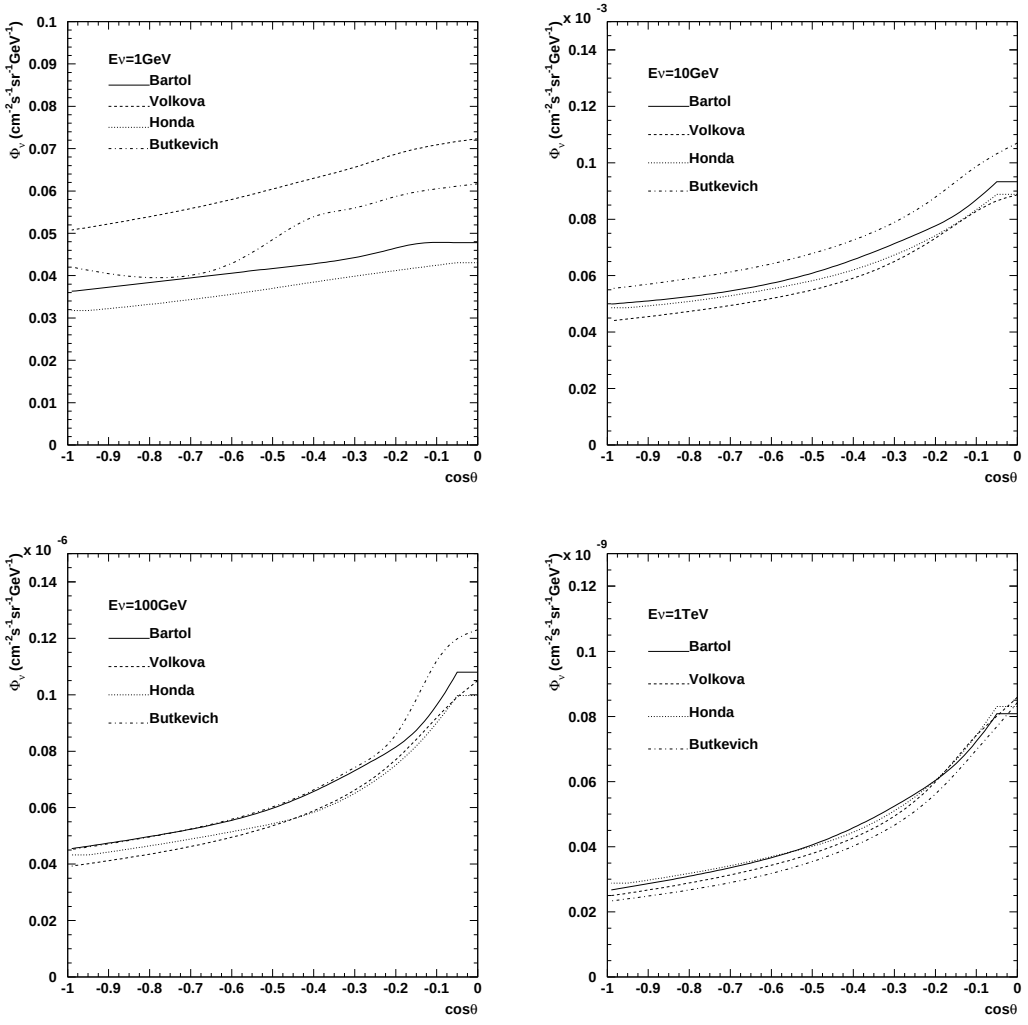

Figure 7.2: The zenith angle distribution of atmospheric neutrino flux in various neutrino energy

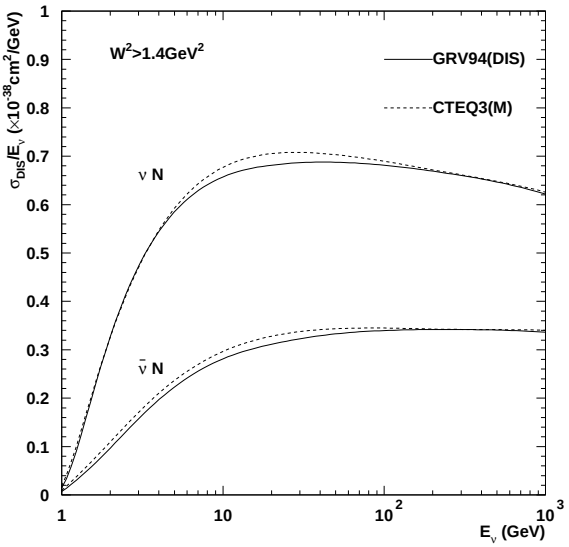

Figure 7.3: $\nu_\mu N$ and $\bar{\nu_\mu} N$ total cross section per neutrino energy

$$F_3 = 2[f_d(f_u) + f_s + f_b - f_{\bar{u}}(f_{\bar{d}}) - f_{\bar{c}} - f_{\bar{t}}] \tag{7.14}$$

$\bar{\nu_\mu} p(n) \rightarrow \mu^+ X$

$$F_2 = 2xF_1 = 2x[f_u(f_d) + f_c + f_t + f_{\bar{d}}(f_{\bar{u}}) + f_{\bar{s}} + f_{\bar{b}}] \tag{7.15}$$

$$F_3 = 2[f_u(f_d) + f_c + f_t - f_{\bar{d}}(f_{\bar{u}}) - f_{\bar{s}} - f_{\bar{b}}] \tag{7.16}$$

There are various kinds of the fitting method with the parton distribution function in order to fit the experimental results. The parton distribution function is limited by minimum momentum transfer Q^2 for correct calculation . Equation 7.12 shows the deep inelastic scattering cross section with large momentum transfer Q^2 and large the invariant mass of final state hadron system. Fig. 7.3 shows the neutrino-nucleon cross section versus neutrino energy. The cross section is obtained by using GRV94(DIS)[17].

7.3.2 Quasi-elastic scattering and single pion production

Total charged current cross section are calculated by D.Rein and LM.Seghal taking into consideration of the quasi-elastic scattering to single pion production. The cross section used in this analysis is shown in Fig. 7.4.

7.4 Energy loss for muons

The neutrino-induced muon goes through in the rock with losing their energy. Its travel length in the rock is calculated to judge whether the muon reaches the detector or not.

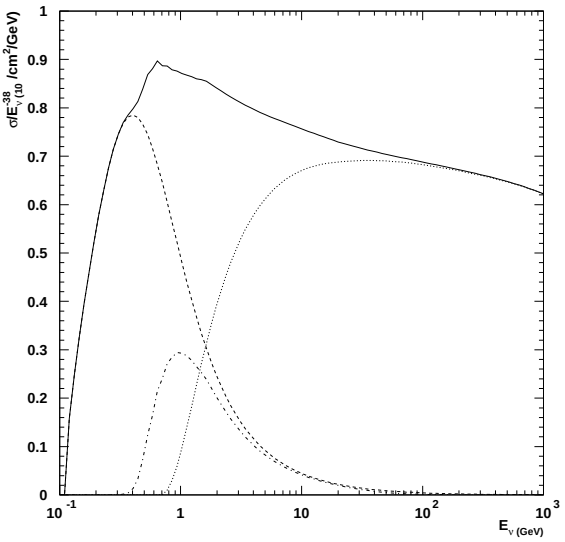

Figure 7.4: Total neutrino-nucleon CC cross section. Dotted line shows the cross section of deep inelastic scattering, dashed line shows one of quasi-elastic scattering, dashed-dot line shows one of single pion production and solid line shows the total cross section

The muon track length in water is calculated for judgment on muons stopping or going through and on muons traveling over 7m.

7.4.1 Muon energy loss in rock

The muon energy loss in rock is calculated by Lohmann, including contributions from bremsstrahlung, direct pair production and photo-nuclear interactions. Fig. 7.5 shows dE/dx in standard rock.

The traveling distance for which muons lose energy down to a threshold E_{th} is calculated from following equation.

$$R(E_\mu, E_{th}) = \int_{E_\mu}^{E_{th}} \frac{-dE}{dE/dX} \tag{7.17}$$

E_{th} defined in this analysis is 1.6GeV and the range with $E_{th} = 1.6$GeV is shown in Fig. 7.6

7.4.2 Muon energy loss in Water

The muon energy loss in water is calculated by Lohmann for muon energy larger than 1 GeV. So Lohmann‘s result is applied for energy loss larger than 1GeV, and ionization energy loss is applied for smaller than 1GeV. The muon range in water is shown in Fig. 7.7. The 7m track length corresponds to a muon energy of 1.6GeV.

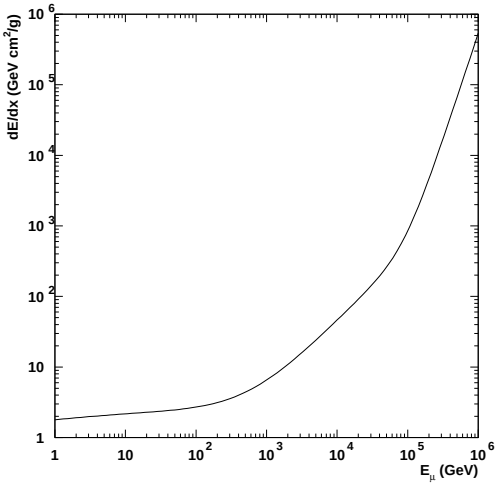

Figure 7.5: dE/dx in standard rock

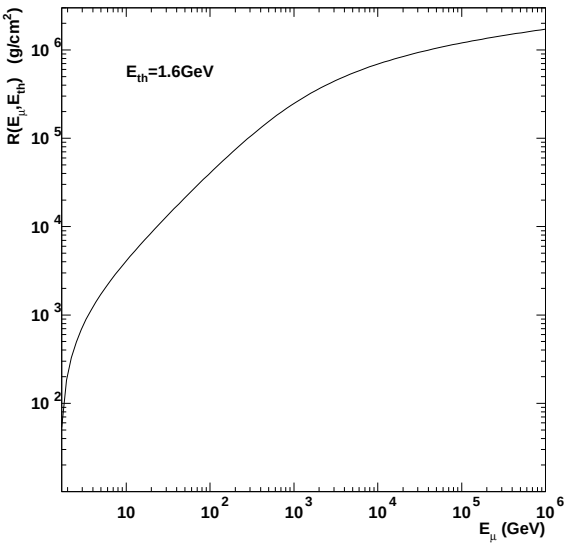

Figure 7.6: Range of muon in standard rock

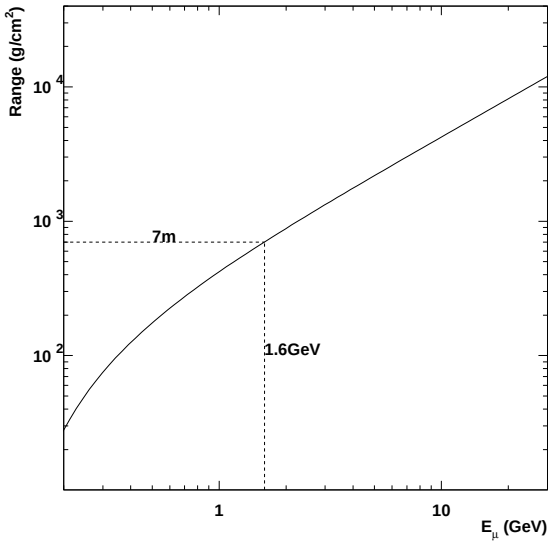

Figure 7.7: Range of muon in water.

7.5 Theoretical uncertainties

In this section, the theoretical uncertainties for the expected upward-going muon flux are described. The uncertainties of atmospheric neutrino flux and neutrino-nucleon interaction are main factor.

7.5.1 Atmospheric neutrino flux

The uncertainty of atmospheric neutrino flux comes from the primary-cosmic ray energy dependence and affects to upward-going muon flux. Although the primary cosmic-ray flux is well studied at low energy, there is large ambiguity in the determination of absolute value. The fitting error of the compilation is obtained to be $\sim$10% for the nucleon flux at 100GeV and $\sim$20% at 100 TeV. The uncertainty in the calculation of the upward-going muon flux is estimated to be approximately $\pm$20% above several GeV.

In addition, the dependencies on neutrino flux model was estimated by comparison of Bartol model[13] with Honda model [15] and shown in Fig 7.8. The uncertainty of absolute flux from model dependence was estimated to be $\sim$ 10%.

Moreover, the zenith angle bin-by-bin uncertainty was estimated by comparison of Bartol model and Honda model. Fig. 7.9 shows the zenith angle bin-by-bin error. The ratio was normalized by the combination of the GRV94 parton distribution function and Bartol neutrino flux model.

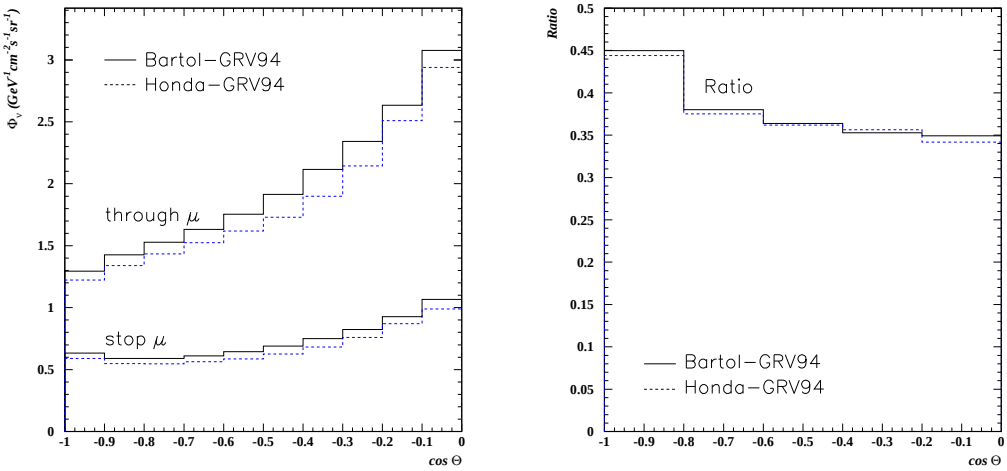

Figure 7.8: Left figure shows the zenith angle distribution of expected upward through-going muon flux and upward stopping muon flux. Right figure shows the zenith angle distribution of the ratio of upward stopping muon to upward through-going muon flux. Solid line shows Bartol model and dashed line shows Honda model.

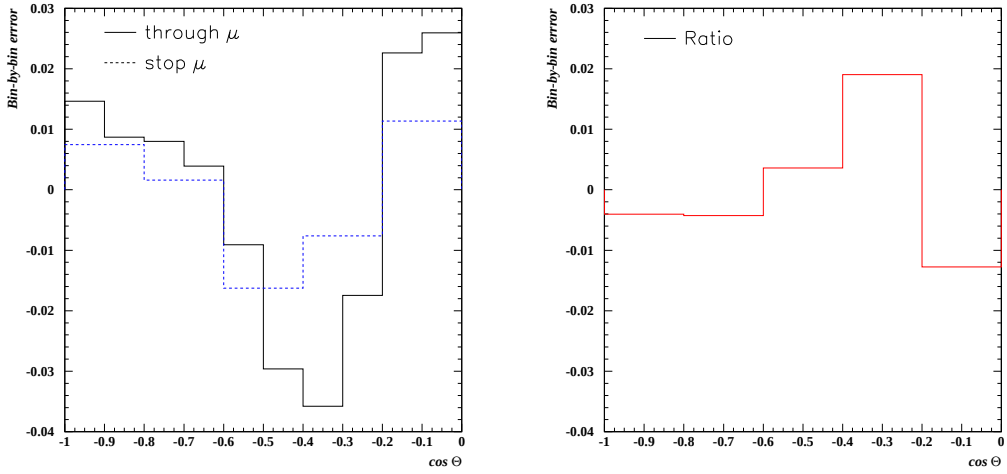

Figure 7.9: The zenith angle bin-by-bin error estimated by model difference. Left figure shows the error of upward stopping muon flux and upward through-going muon flux. Right figure shows the error of the ratio of upward stopping muon flux to upward through-going muon flux. These ratio are normalized by the combination of the GRV94 and Bartol model.

7.5.2 The ratio of upward stopping muon flux to upward through-going muon flux

The ratio of upward stopping muon flux to upward through-going muon flux is useful for the analysis. Because the neutrino flux is approximately defined as (absolute flux)$\times E_\nu^{-\gamma}$ and the cross section of the deep inelastic scattering is canceled, the large uncertainty in the neutrino flux normalization and the neutrino interaction cross section were canceled.

The uncertainty of atmospheric neutrino flux comes from the primary-cosmic ray energy dependence and affects to upward-going muon flux. To estimate the uncertainty of the upward-going muon flux, the change of energy spectrum for atmospheric neutrino is applied as follows,

$$\frac{d\phi_\nu}{dE_\nu} \rightarrow \frac{d\phi_\nu}{dE_\nu} \times E_\nu^{\pm 0.05} \tag{7.18}$$

The uncertainty of the ratio of upward stopping muon flux to upward through-going muon flux come from the uncertainty of the spectrum index is estimated to be +12.5% -11.4%.

Described as before, the uncertainty of the total charged current cross section only consider quasi-elastic scattering and single pion production. When the cross section is changed with ± 15%, the change of upward-going muon flux is estimated to be +4.2% -3.5%.

7.6 Expected flux of upward going muons

The upward-going muon flux are calculated by using Bartol's atmospheric neutrino flux[13] and GRV94 neutrino-nucleon neutrino interaction[17]. The energy loss for muons are applied with Lohmann's calculation [18]. The expected upward-going muon flux ($E_\mu >$ 1.6GeV) is

upward stopping muon flux	:	0.73 ± 0.16(theo.) ($\times 10^{-13}$cm^{-2}s^{-1}sr^{-1})
upward through-going muon flux	:	1.97 ± 0.44(theo.) ($\times 10^{-13}$cm^{-2}s^{-1}sr^{-1})
upstop/upthru ratio	:	$0.37^{+0.049}_{-0.04}$(theo.)
total upward-going muon flux	:	2.70 ± 0.47(theo.) ($\times 10^{-13}$cm^{-2}s^{-1}sr^{-1})

Chapter 8

Neutrino Oscillation

The neutrino oscillation is described in Section 1.1. In this chapter observed and expected flux are applied to the analysis of neutrino oscillation. $\nu_\mu \rightarrow \nu_\tau$ oscillation is considered as the most probable process of neutrino oscillation analysis described in Section 1.1. The three kinds of oscillation result are estimated, for upward through-going muon, the ratio of upward stopping muon to upward through-going, upward stopping muon and through-going combined.

8.1 Method to examine neutrino oscillations

The basic oscillation examination is done by comparison between the observed result and the expected. The χ^2 examination is applied to the oscillation analysis in this study. The χ^2 examination is done at the various oscillation parameter, Δm^2 and $\sin^2 2\theta$, and the best fit parameter at minimum χ^2 is searched.

The basic χ^2 definition for oscillation analysis is written in,

$$\chi^2 = \sum \left(\frac{N_{obs} - (1+\epsilon)N_{exp}}{\sigma_{N_{err}}} \right)^2 + \sum \left(\frac{\epsilon}{\sigma_\epsilon} \right)^2 \tag{8.1}$$

where N_{obs} is observed value, N_{exp} is expected, N_{err} is the sum of observed and expected error including statistic and systematic error, ϵ is normalization factor, and σ_ϵ is the error of the normalization factor. We divided the data into 10 zenith angle bin for upward through-going muon, 5 for the ratio of stopping muon to through-going muon, 15 for combined upward stopping and through-going muon analysis. The range of the oscillation parameter is $0 \leq \sin^2 2\theta \leq 1$ and $10^{-4} \leq \Delta m^2 \leq 1$ examined, this region is divided into 1763 points. The oscillated expected flux are calculated from Equation 1.8 and Equation 1.9.

8.2 Effect on oscillation analysis from theoretical uncertainties

The observed and expected systematic error and normalization factor are described. The most dominant systematic error comes from the absolute normalization of atmospheric neutrino flux with error $\sim 20\%$.

The systematic uncertainties are shown in Table 8.1 and the normalization summary for oscillation analysis is shown in Table 8.2.

(a)Theoretical uncertainties in flux calculation

typical ν flux normalization	$\pm$20.0%
choice of ν flux/PDF	$\pm$10.0%

(b)Stop/thru theoretical uncertainties

primary spectrum index	+12.5% -11.4%
cross section	+4.2% -3.5%
choice of ν flux	$\pm$0.9%

(c)Experimental sys. errors in through flux

7m track length cut	$\pm$0.5%
live time	$\pm$1.0%

(d)Experimental sys. errors in stopping flux

7m track length cut	+4.9% -4.1%
live time	$\pm$1.0%

(e)Experimental stop/thru sys. errors

7m track length cut	$\pm$4.9%
live time	$\pm$1.0%
stop/thru miss ID	$\pm$1.0%

Table 8.1: Uncertainties for oscillation analysis.

absolute normalization factor σ_α	22.4%
stop/thru relative normalization factor σ_β	14.2%
atmospheric K/π ratio normalization factor σ_ϵ	3%

Table 8.2: The systematic error of normalization factor for oscillation analysis.

8.3 $\nu_\mu \rightarrow \nu_\tau$ oscillation

The three kinds of oscillation analysis results are shown as follows.

The χ^2 definition of through-going muon is as follows,

$$\chi^2 = \sum_{i=1}^{10(thru)} \left(\frac{(\frac{d\Phi}{d\Omega})^i - (1+\alpha)(1+2\varepsilon(\cos\Theta_i + 0.5))(\frac{d\Phi}{d\Omega})^i_{theo}(\sin^2 2\theta, \Delta m^2)}{\sqrt{(\sigma^i_{stat})^2 + (\sigma^i_{sys})^2}} \right)^2 + \left(\frac{\alpha}{\sigma_\alpha}\right)^2 + \left(\frac{\varepsilon}{\sigma_\varepsilon}\right)^2 \quad (8.2)$$

where $\left(\frac{d\Phi}{d\Omega}\right)^i$ is observed muon flux in the i-th cosΘ, $\left(\frac{d\Phi}{d\Omega}\right)^i_{theo}$ is theoretical muon flux, $\sigma^i_{\rm stat}$ is experimental statistical error, $\sigma^i_{\rm sys}$ is bin-by-bin uncorrelated theoretical and experimental systematic errors, α is absolute flux normalization factor with error σ_α, ϵ is vertical/horizontal correlated normalization factor with error σ_ϵ. The zenith angle distribution of through-going muon flux and the confidence intervals for $\nu_\mu \rightarrow \nu_\tau$ oscillations is shown in Fig.8.1.

The χ^2 definition of the ratio of stopping/through-going muon is as follows,

$$\chi^2 = \sum_{i=1}^{5(ratio)} \left(\frac{R^i - R^i_{theo}(\sin^2 2\theta, \Delta m^2) \times (1+\beta)}{\sqrt{\left(\sigma^i_{R_{stat}}\right)^2 + \left(\sigma^i_{R_{sys}}\right)^2}} \right)^2 + \left(\frac{\beta}{\sigma_\beta}\right)^2 \quad (8.3)$$

where R^i is the observed flux ratio in the i-th cosθ, $R^i_{\rm theo}$ is the theoretical muon flux ratio, and β is the relative normalization factor for the ratio of stopping muon flux to through-going flux with error σ_β. The vertical/horizontal normalization factor is almost canceled. The zenith angle distribution of the ratio and confidence interval are shown in Fig.8.2.

The χ^2 definition of combined stopping and through-going muon is as follows,

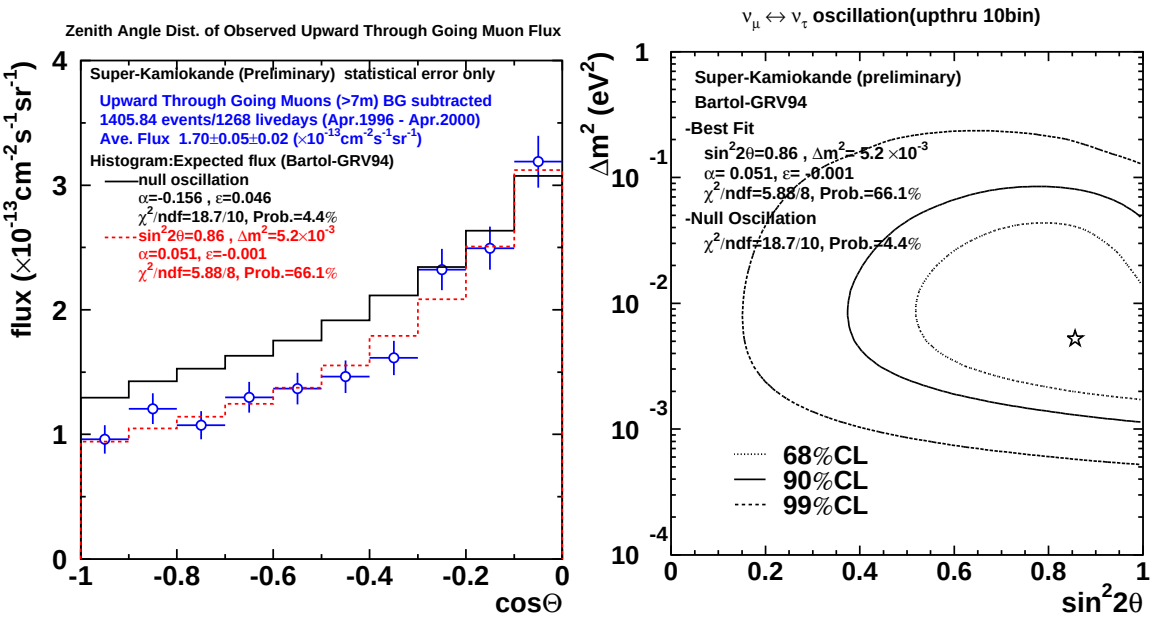

Figure 8.1: Oscillation result for through-going muon flux. The left figure shows the zenith angle distribution and the right shows the confidence interval.

$$
\begin{aligned}
\chi^2 = & \\
& \sum_{i=1}^{10(thru)} \left(\frac{(\frac{d\Phi}{d\Omega})^i - (1+\alpha)(1+2\varepsilon(\cos\Theta_i + 0.5))(\frac{d\Phi}{d\Omega})^i_{theo}(\sin^2 2\theta, \Delta m^2)}{\sqrt{(\sigma^i_{stat})^2 + (\sigma^i_{sys})^2}} \right)^2 \\
& + \sum_{i=1}^{5(stop)} \left(\frac{(\frac{d\Phi}{d\Omega})^i - (1+\alpha)(1+\beta)(1+2\varepsilon(\cos\Theta_i + 0.5))(\frac{d\Phi}{d\Omega})^i_{theo}(\sin^2 2\theta, \Delta m^2)}{\sqrt{(\sigma^i_{stat})^2 + (\sigma^i_{sys})^2}} \right)^2 \\
& + \left(\frac{\alpha}{\sigma_\alpha}\right)^2 + \left(\frac{\beta}{\sigma_\beta}\right)^2 + \left(\frac{\varepsilon}{\sigma_\varepsilon}\right)^2 \qquad (8.4)
\end{aligned}
$$

The zenith angle distribution for stopping and through-going muon flux is shown in Fig.8.3 and the confidence interval is shown in Fig.8.4.

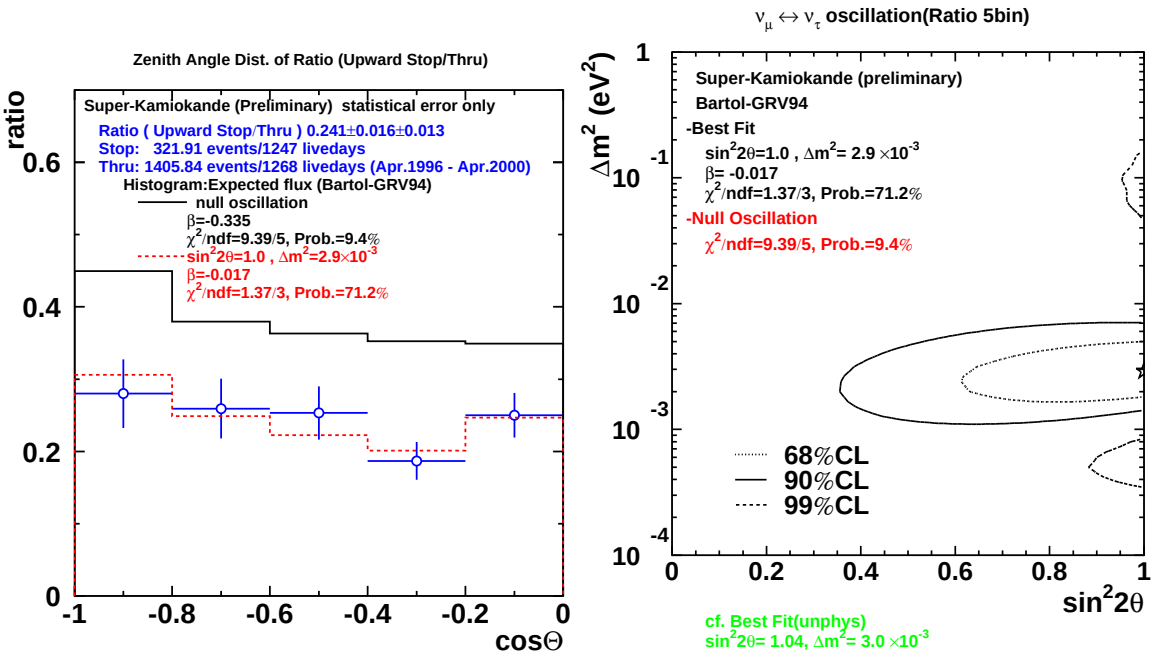

Figure 8.2: Oscillation result for the stop/through ratio. The left figure shows the zenith angle distribution of the ratio and the right shows the confidence interval of the ratio.

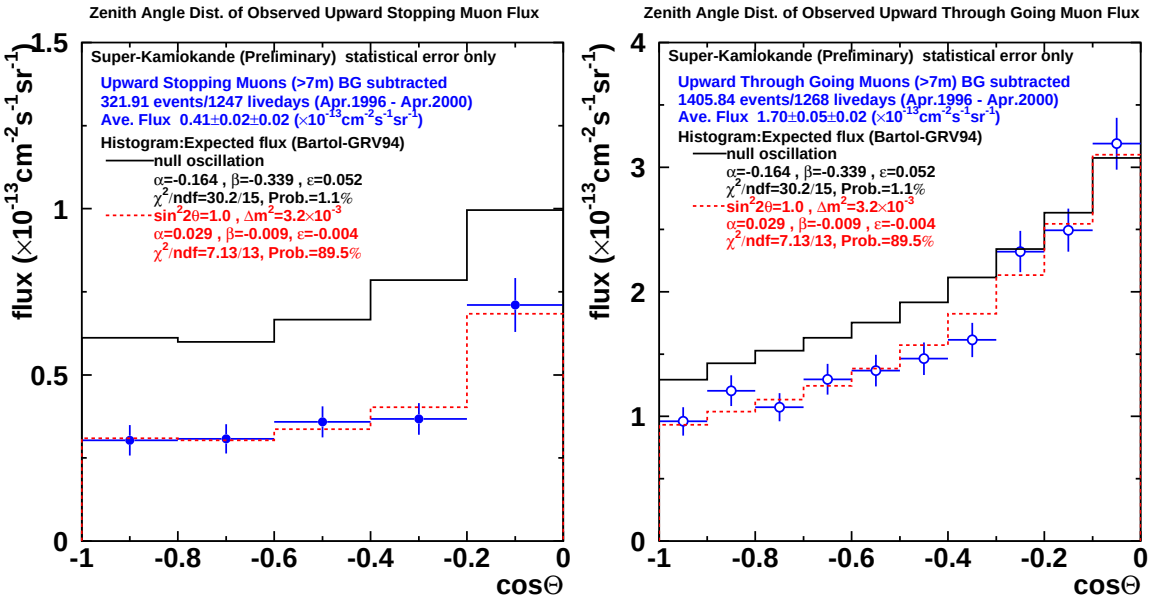

Figure 8.3: Zenith angle distribution of upward muon flux. The left figure shows stopping muon flux and the right shows through-going muon one.

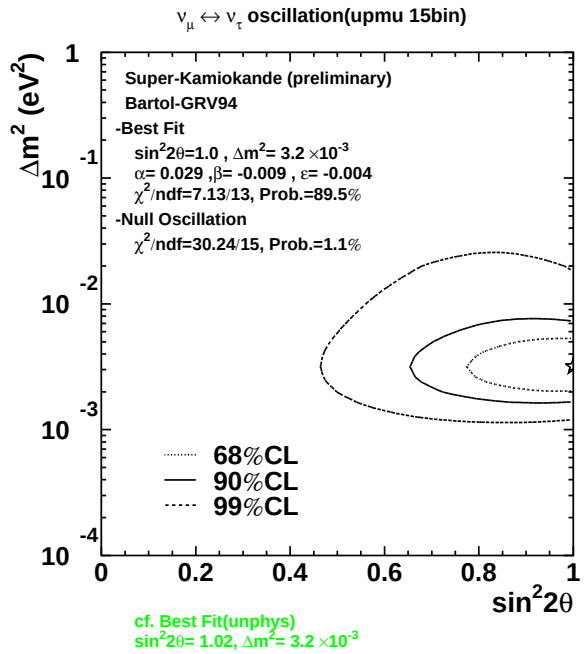

Figure 8.4: Confidence interval for combined stopping muon and through-going muon.

Chapter 9

Approach with Monte Carlo simulation

The upward-going muon flux was calculated by analytical calculation method, but there are no consider for angle of neutrino-nucleon interaction, the multiple scatter of muons, neutral current effect and the precise detector response. The Monte Carlo approach is good solution for these problems.

9.1 Monte Carlo method for upward-going muons

- Atmospheric neutrino flux
  The Bartol model[13] is applied for atmospheric neutrino flux same as analytical calculation described in Section 7.2. The neutrino energy range is applied from 1.6GeV to 90TeV.

- Neutrino-nucleon cross section
  The neutrino-nucleon interaction is applied as same as analytical calculation described in Section 7.3. So the cross section is calculated by using GRV94 parton distribution function[17]. The only charged current interaction is generated out of the detector and both charged current interaction and neutral current are generated in the detector.

- Area of the neutrino-nucleon interaction point
  The area that the neutrino-nucleon interaction is generated is in the spherical shape with 4km radius, the detector is located at center of the sphere.

- Detector simulator
  The GEANT program in CERN program library is used for detector simulation commonly used in high-energy experiments.

- Muon energy loss
  The muon energy loss is applied the Lohmann's model[18], same as analytical calculation.

- Data selection
  The data selection is done by true information, judgment between stop and thru, and 7m track length cut and zenith angle cut are applied.

9.2 Comparison between MC and analytical calculation

The live time 19.5years Monte Carlo data was generated. The Monte Carlo result and analytic calculation result are compared in the absolute flux and the zenith angle distribution of the flux.

The comparison result for upward stopping muon flux is shown in Fig. 9.1. The left-side figure shows the zenith angle distribution for upward stopping muon flux, the cross shows Monte Carlo flux and the solid line shows analytic calculation flux. The absolute flux for upward stopping muon is $0.73 \pm 0.02(\text{stat.})(\times 10^{-13}\text{cm}^{-2}\text{s}^{-1}\text{sr}^{-1})$ for Monte Carlo and $0.73(\times 10^{-13}\text{cm}^{-2}\text{s}^{-1}\text{sr}^{-1})$ for analytic calculation obtained, both flux are consistent. The right-side figure shows the zenith angle shape difference, upper figure shows normalized flux distribution and lower figure shows the ratio of Monte Carlo to analytic calculation, and the shape is found to be consistent.

The comparison result for upward through-going muon flux is shown in Fig. 9.2. The absolute flux is $1.89 \pm 0.02(\text{stat})(\times 10^{-13}\text{cm}^{-2}\text{s}^{-1}\text{sr}^{-1})$ for Monte Carlo and $1.97(\times 10^{-13}\text{cm}^{-2}\text{s}^{-1}\text{sr}^{-1})$ for analytic calculation. The Monet Carlo absolute flux is smaller than analytic calculation with 4%. From The right-side and lower figure, the shape is found to be consistent.

The comparison result for upward stop/through ratio is shown in Fig. 9.3. The absolute ratio is $0.39 \pm 0.01(\text{stat.})$ for Monte Carlo and 0.37 for analytic calculation, the absolute difference is 4% which come from the inconsistent of through-going muon result. The shape is found to be consistent.

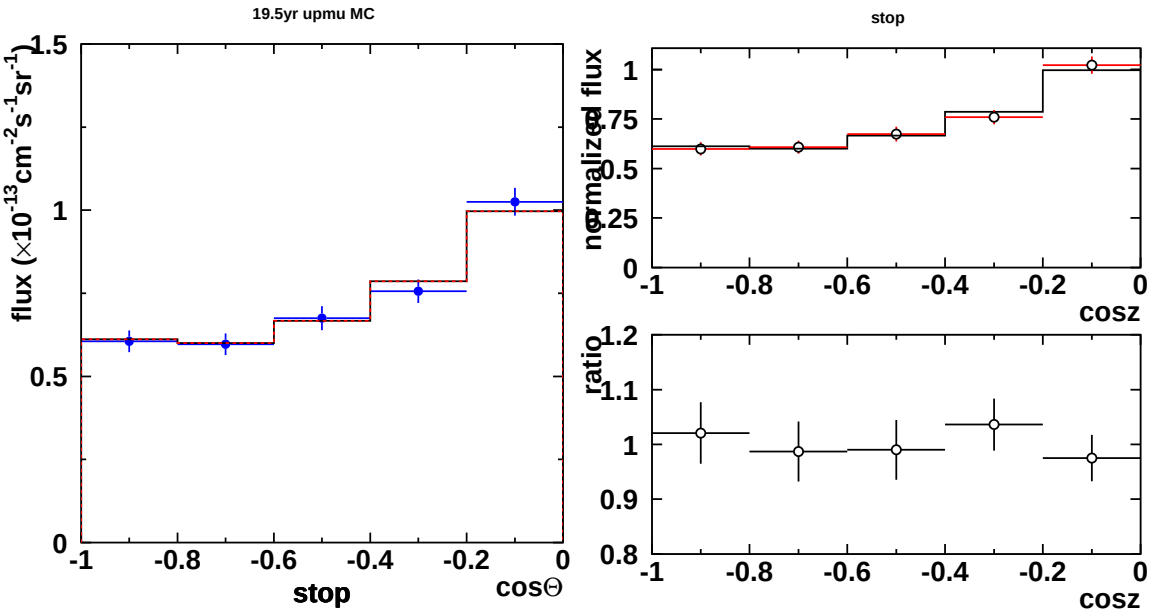

Figure 9.1: Upward-stopping muon flux

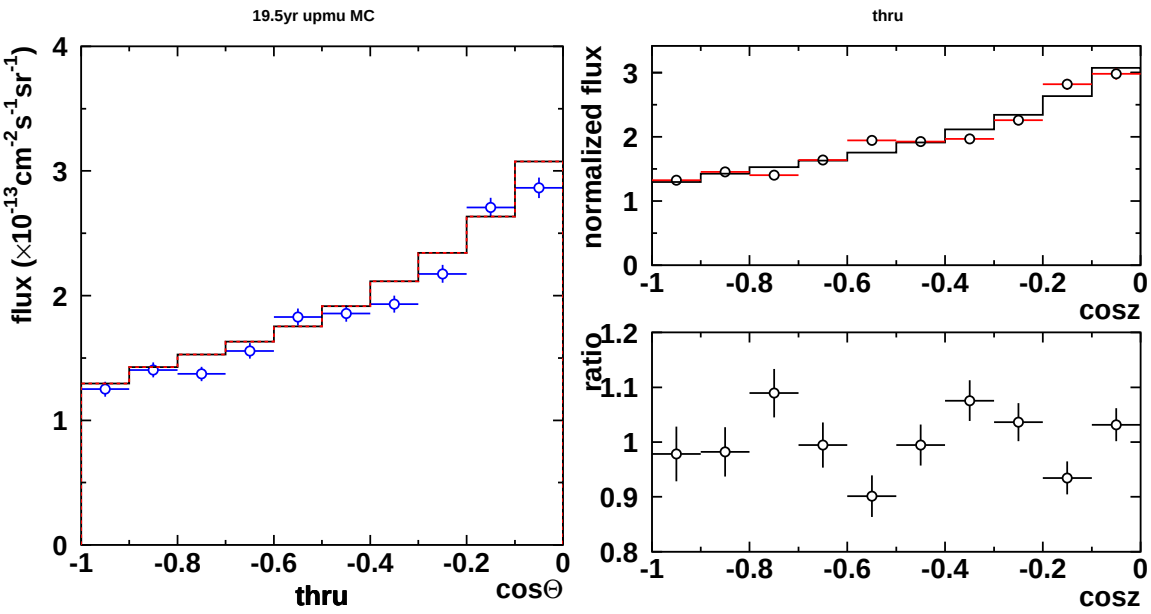

Figure 9.2: Upward through-going muon flux

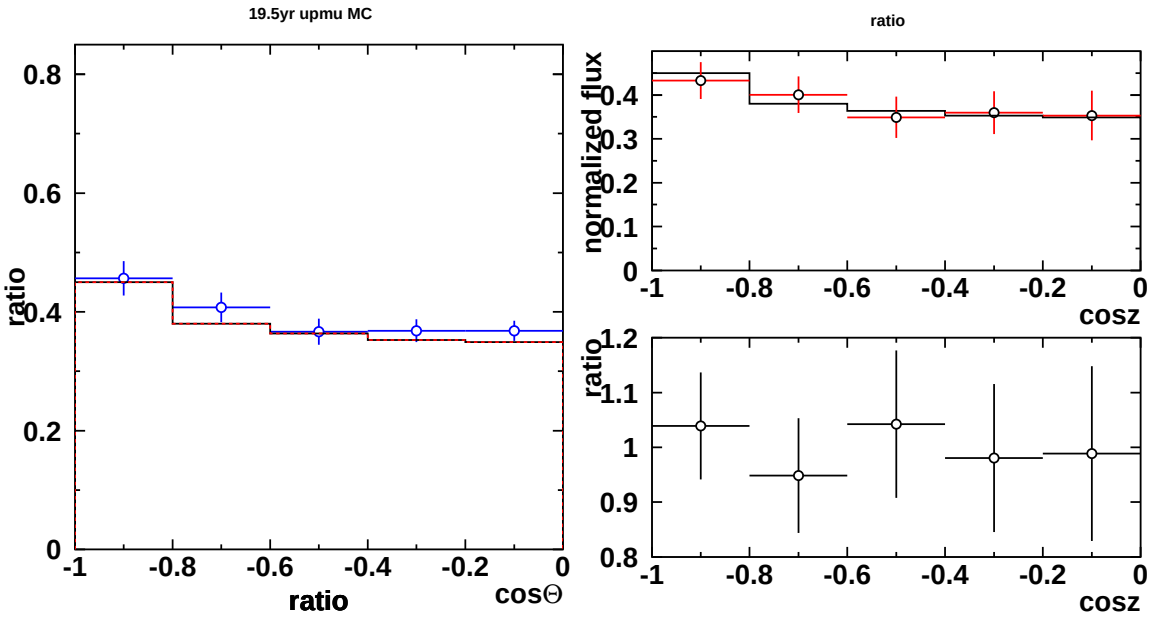

Figure 9.3: The ratio of upward stopping muon flux to upward through-going muon flux

Chapter 10

Atmospheric $\nu/\bar{\nu}$

10.1 Method to estimate atmospheric $\nu/\bar{\nu}$

The upward-going muons detected in Super-Kamiokande is generated by simple process of neutrino-nucleon charged current interaction as follows,

$$\nu + \mathrm{N} \rightarrow \mu^- + \mathrm{X} \tag{10.1}$$

$$\bar{\nu} + \mathrm{N} \rightarrow \mu^+ + \mathrm{X} \tag{10.2}$$

where N is nucleon and X is any particle. Then the relation between atmospheric $\nu_\mu/\bar{\nu}_\mu$ and the charge ratio of neutrino induced upward stopping muons is as follows,

$$\frac{\phi_{\nu_\mu}}{\phi_{\bar{\nu}_\mu}} = \frac{\sigma_{\bar{\nu}N}}{\sigma_{\nu N}} \frac{N_{\mu^-}}{N_{\mu^+}} \tag{10.3}$$

where ϕ_ν,$\phi_{\bar{\nu_\mu}}$ is the atmospheric neutrino flux for ν, $\bar{\nu}$ respectively and $\sigma_{\nu N}, \sigma_{\bar{\nu}N}$ are cross section of $\nu N, \bar{\nu} N$ in charged current interaction. N_{μ^-} and N_{μ^+} are number of μ^- and μ^+, respectively. We compare experimental data with theoretical value for the atmospheric neutrino and anti-neutrino ratio as follows,

$$\frac{(\phi_\nu/\phi_{\bar{\nu}})_{data}}{(\phi_\nu/\phi_{\bar{\nu}})_{theo.}} = \frac{(N_{\mu^-}/N_{\mu^+})_{data}}{(N_{\mu^-}/N_{\mu^+})_{theo.}} \tag{10.4}$$

The theoretical atmospheric neutrino ratio is estimated by using analytical calculation as follows,

$$\frac{\int \phi_\nu(E_\nu) \times D \times \sigma_{\nu N}(E_\nu) \times \, dE_\nu}{\int \phi_{\bar{\nu}}(E_{\bar{\nu}}) \times D \times \sigma_{\bar{\nu}N}(E_{\bar{\nu}}) \times \, dE_{\bar{\nu}}} = \frac{N_{\mu^-}}{N_{\mu^+}} \tag{10.5}$$

where D is nucleon density of rock and E_ν is neutrino energy.

10.2 Charge separation of muons

Although the charged particles is usually separated by magnetic field in accelerator experiments, directly separation of charged particle is impossible for the Super-Kamiokande.

In this study, charge difference is observed by using lifetime difference of muons in water. The lifetime for muons in Super-Kamiokande is obtained by observation the time difference between parent muon and decay electron. Charge ratio for upward going muons is equivalent to the ratio of the number of μ^+ to μ^- after correction of nuclear absorption for μ^-.

In vacuum, both μ^+ and μ^- have same lifetime, 2.2μsec [19]. However, μ^+ and μ^- have different lifetime in water because of only μ^- captured by medium atom($\mu^- + p \rightarrow n + \nu_\mu$). Then μ^- has shorter lifetime than μ^+[20]. The lifetime of each muons in water is as follows,

$$\tau_{\mu^-} = 1.17954 \pm 0.0020\mu\text{sec}$$
$$\tau_{\mu^+} = 2.19703 \pm 0.00004\mu\text{sec}$$

Therefore the muon counts of the mixture of two muons which have different lifetime in a water. The number of the particle with lifetime τ is shown as equation(10.6).

$$N(t) = N_0 exp\left(-\frac{t}{\tau}\right) \tag{10.6}$$

where N_0 is number of particle at t=0, and $N(t)$ at t=t.

The two kind of method for estimation N_{μ^-}/N_{μ^+} are available, the lifetime fitting method and lifetime ratio method. The former lifetime fitting method is using the decay curve for time difference between muon and decay electron.

At first decay rate of the particle $-dN(t)/dt$ is expressed as following equation(10.6).

$$-\frac{dN(t)}{dt} = \frac{N_0}{\tau} exp\left(-\frac{t}{\tau}\right) \tag{10.7}$$

In the next step, the number of count(N_{count}) during Δt is as follows,

$$\begin{aligned} N_{count}(t \sim t + \Delta t) &= \int_t^{t+\Delta t} \left(-\frac{dN(t)}{dt}\right) dt \\ &= N_0 \left[1 - exp\left(-\frac{\Delta t}{\tau}\right)\right] exp\left(-\frac{t}{\tau}\right) \end{aligned} \tag{10.8}$$

The number of count is estimated separately by equation(10.8) for μ^-,μ^+. The total number of count(N_{total}) is shown as following equation10.9.

$$\begin{aligned} N_{count}(t \sim t + \Delta t) &= N_{\mu^+} \left[1 - exp\left(-\frac{\Delta t}{\tau_{\mu^+}}\right)\right] exp\left(-\frac{t}{\tau_{\mu^+}}\right) \\ &\quad + N_{\mu_-} \left[1 - exp\left(-\frac{\Delta t}{\tau_{\mu^-}}\right)\right] exp\left(-\frac{t}{\tau_{\mu^-}}\right) \end{aligned} \tag{10.9}$$

The tuning parameters in the equation 10.9 are N_{μ^-} and N_{μ^+}.

In order to deduce the true charge ratio of muons observed in the SK detector, we should taken into the μ^- nucleon capture in water. There is no electron emission when nuclear μ^- capture occurred. Λ_c(the nucleon capture ratio) is defined for oxygen as follows[20],

$$\Lambda_c = 0.184 \pm 0.001$$

Finally, the charge ratio of muons($R(\mu^+/\mu^-)$) turns out to be,

$$R(\mu^+/\mu^-) = \frac{N_{\mu^+}}{N_{\mu^-}/(1-\Lambda_c)} \tag{10.10}$$

Since only tagged decay electron events is used in the lifetime fitting method, the large amount of events are required and it is not suitable for this analysis. Therefore, latter method, lifetime ratio method is adopted.

The lifetime ratio method uses all event detected stopping muons. Although the lifetime ratio method is basically same as lifetime fitting method, the charge ratio is estimated by integrating the Eqn. 10.9 and Eqn. 10.10.

At first, we defined the ratio of number of μ^+ and μ^- as $N_{\mu^+} : N_{\mu^-} = 1 : X$. The ratio of the number of total muons to electron tagged events which lifetime is longer than definite time ($N_{e-tag}/N_{total\mu}$) is shown as follows,

$$\frac{N_{e-tag}}{N_{total\mu}} = \frac{\epsilon_{\mu^+}\,(exp(-T/\tau_{\mu^+}) + Xexp(-T/\tau_{\mu^-})(1-\Lambda_c))}{1+X} \tag{10.11}$$

where ϵ_{μ^+} is the detection efficiency for μ^+ and T is definite time. The ratio $N_{e-tag}/N_{total\mu}$ is obtained experimentally.

10.3 Event selection

10.3.1 Parent upward stopping muons

Contamination of cosmic-ray muons

The contamination of cosmic-ray is described in Section 5.5 The contamination due to the cosmic-ray muons exists only between $-0.1 \leq \cos\Theta \leq 0$ (Θ:vertical angle) in zenith angle direction. Therefore events in the region $60^o \leq \phi$(azimuth angle) $\leq 310^\circ$ and $-0.1 \leq \cos\Theta(\Theta$: vertical angle) ≤ 0 are removed from the data set.

Fiducial volume cut

Fiducial volume cut is applied on the muon events. This cut requires that stopping position of muons should be away more than 2m from detector wall as shown in Fig. 10.1. This cut is useful for rejection γ-ray events which is generated frequency available near the wall (Fig. 10.1) and affects destructively the detection efficiency for decay electron in the analysis. Although almost noises near the wall are eliminated by time difference cut by coincidence between parent muon and decay electron, we applied this cut because of well known energy resolution for the decay electron in fiducial volume.

10.3.2 Electron from decayed muon

In this section, the direction and vertex reconstruction for μ decay electron is described. Figure 10.2 is the typical event of μ decay electron.

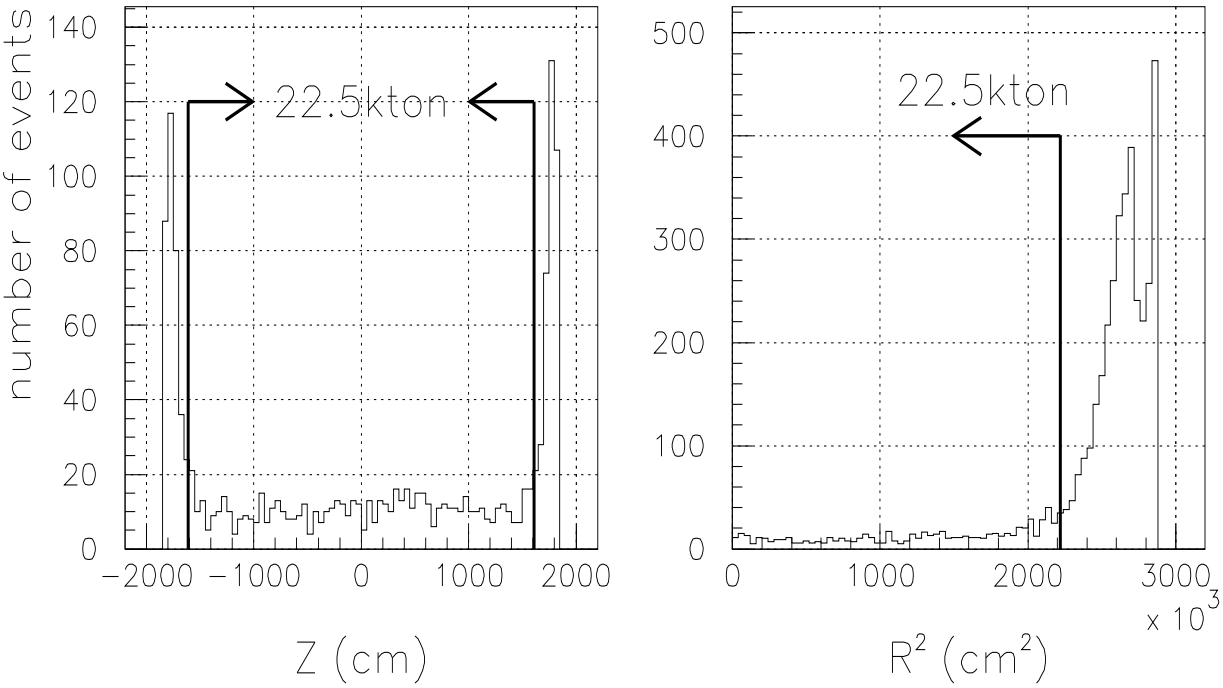

Figure 10.1: The vertex distribution for low energy events. The left-side plot is Z distribution(+18.1m and -18.1m show the top and bottom PMT) and the right-side plot is R(radial direction). The large amount of events are found near inner-detector wall. The fiducial volume away more than 2m from detector wall is 22.5kton.

Vertex reconstruction

At first, the hit channel is selected for vertex reconstruction as below. The time distribution of hit PMTs is shown in Fig. 10.3. The peak around 900nsec is the signal of electron event and noise signals by dark current of PMTs are found after 1200nsec. The noise signal deteriorates the vertex reconstruction. Accordingly it is eliminated as follows.

1. The 200nsec timing window is determined so as to include maximum hit PMTs. In the Figure10.3, this window is between t_2 and t_3.

2. The number of background hit in the timing window is estimated using following equation.

$$N_{background} = (t_2 - t_3)\frac{N_{hit}(t_1 : t_2) + N_{hit}(t_3 : t_4)}{(t_2 - t_1) + (t_4 - t_3)} \tag{10.12}$$

3. 200nsec window is divided to 11 small window and significance for each small window is calculated as follows,

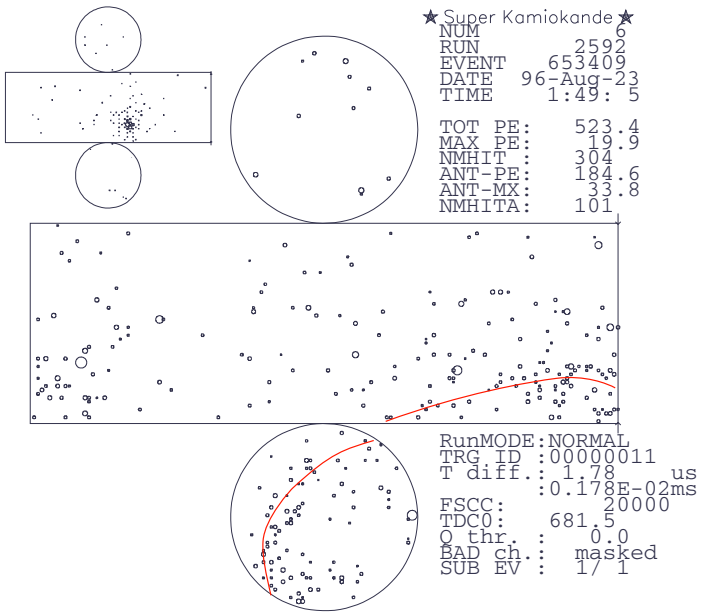

Figure 10.2: Typical μ decay electron event. solid line shows the result of vertex and direction reconstruction.

$$significance = \frac{N_{signal}}{\sqrt{N_{background}}} \tag{10.13}$$

where N_{signal} is equivalence to $N_{hit} - N_{background}$.

4. Select the small window which has maximum significance.

5. The other small window which the significance is larger than 80% of maximum significance is selected and use for vertex reconstruction.

Next, reconstruct the vertex point using selected channel by the grid search method described as Section 5.2.1. The function for vertex reconstruction is Eqn. 10.14 and search minimum point for T^2.

$$T^2 = \sum_{i=1}^{N_{hit}} t^2_{resolution,i} \tag{10.14}$$

where $t_{resolution,i}$ is the time which difference time between detected time at PMT and time of flight of photon, $t_{resolution,i}$ is defined as follows,

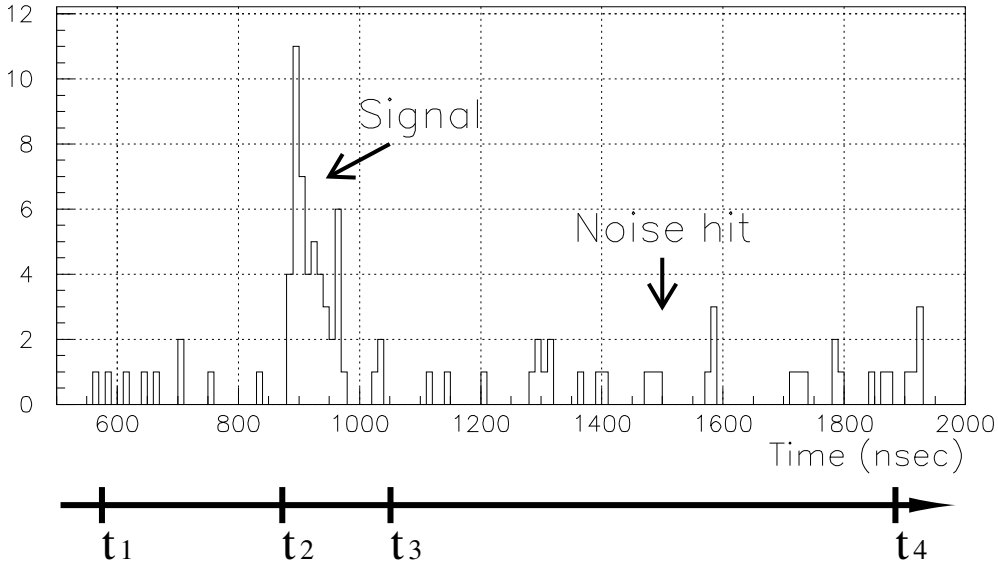

Figure 10.3: Timing distribution of electron event

$$t_{resolution,i} = t_i^0 - (n/c) \times \sqrt{(x-x_i)^2 + (y-y_i)^2 + (z-z_i)^2} - t_c \tag{10.15}$$

t_i^0 : hit time at i-th PMT
n : refraction index ($n = 1.34$ in water)
c : velocity of photon in vacuum
(x, y, z) : vertex point of decay electron
(x_i, y_i, z_i) : location of i-th PMT
t_c : average of t_i

Goodness is defined by the time resolution of PMT as follows,

$$goodness = \frac{1}{\Sigma\frac{1}{\sigma_i^2}} \times \Sigma\frac{1}{\sigma_i^2} exp\left[-\frac{t_{resolution,i}^2}{2\sigma_i^2}\right] \tag{10.16}$$

where σ_i is time resolution of PMT. The goodness takes the value between 0 and 1. If $t_{resolution,i}$ is 0, goodness takes 1. The method of grid search is same as muons case and determines the point where goodness takes maximum value.

Table10.1 shows vertex reconstruction resolution described in Section 5.2.1. The vertex position and resolution is estimated from average and σ by Gaussian fitting as figure10.4. Then σ_r is estimated from difference distribution(figure10.4) as the region including 68% of all.

Position (x,y,z)	$\triangle x$	$\triangle y$	$\triangle z$	σ_x	σ_y	σ_z	σ_r
(35.3,-70.7,-1200)	-0.3	-2.7	-3.0	47.98	49.28	47.66	115.8
(35.3,-70.7,0)	0.7	-0.5	-1.9	47.11	49.23	52.80	114.2
(35.3,-70.7,1200)	-1.0	-0.7	-1.0	46.87	48.17	47.88	113.6
(35.3,-70.7,1600)	-0.6	-2.8	-10.0	46.98	46.40	44.67	111.6
(35.3,-1201,-1200)	-3.4	7.0	-7.0	46.91	47.65	47.40	110.7
(35.3,-1201,0)	-1.1	16.0	-1.1	42.70	43.16	50.08	113.0
(35.3,-1201,1200)	0.6	10.0	2.0	43.74	44.92	48.74	109.4

Table 10.1: Vertex reconstructed position difference and resolution by Ni calibration

Energy spectrum for electron

Characteristics for muon decay is the maximum 50MeV in energy spectrum. The determination of energy is on the different basis between low energy event like electron and high energy event like muon. The energy in high energy event is determined by using

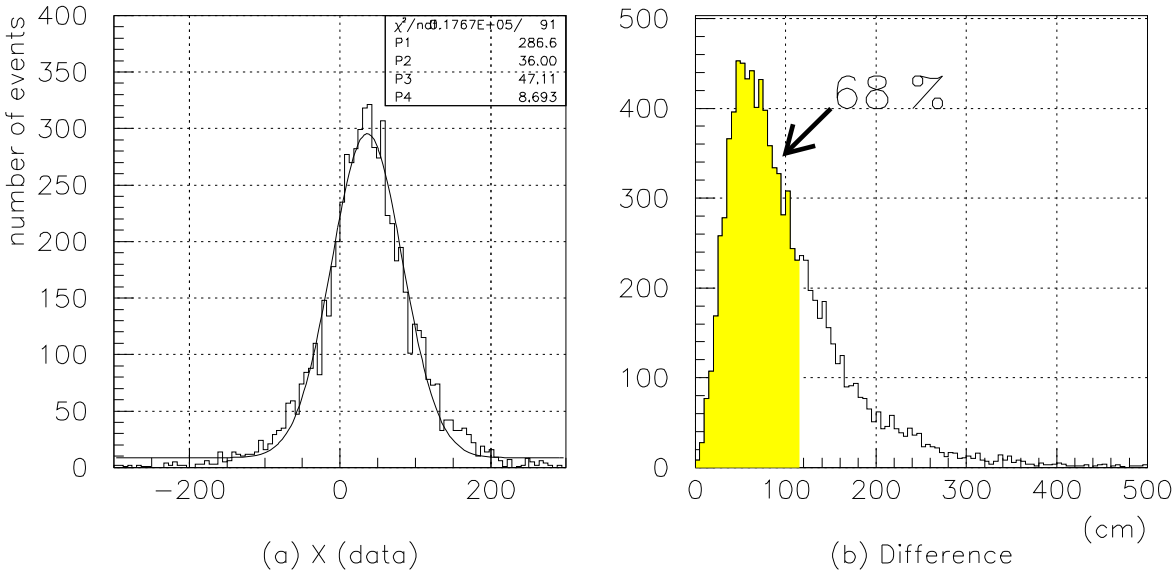

Figure 10.4: The resolution of vertex reconstruction for electron

total charge of hit PMTs. On the other hand, in the low energy case, determined by the number of hit PMTs. Since the amplifier of PMT is not stable in low energy, definition of number of hit PMT is better than definition of charge.

In order to reject the dark noise events of PMTs, the corrected number of hit N_{50} is defined which applied corrections of tube weights taking into account of the attenuation, geometry, and charge corrections. The N_{50} has a good energy scale in low energy as characteristic value of the event.

μ decay electron events

Backgrounds for decay electron are radioactivity in water and γ-ray from rock, electric noise. Following event selection was applied in order to eliminate these background.

μ decay electron Event selection

These electron events are emitted after parent muons released that's energy and stopped. Since the lifetime of muon in vacuum is 2.2μsec, events which have time difference between muon and following event is shorter than 30μsec was collected.

Goodness cut

The definition of goodness was described elsewhere and is used for inspection of quality for vertex reconstruction. This definition is also used for decay electron. For decay electron selection, goodness is used for elimination of electrical after-pulse due to parent muon. Event with goodness > 0.5 is taken into data set.

Energy cut

Fig. 10.5 shows energy distribution for decay electron of muon. MC and experimental data is consistent with the data around 5MeV except very low energy region. The difference comes from gamma-ray by radioactivity element in the water and μ^- nucleon capture by nucleus. Stopping μ^- is sometimes captured by Oxygen atom in the water and excited to ^{16}N. When excited ^{16}N goes to ground state, emitted gamma-ray. The maximum energy of emitted gamma-ray is 10.8MeV. Then $N_{50} > 60$ was applied effectively for rejection these noise events.

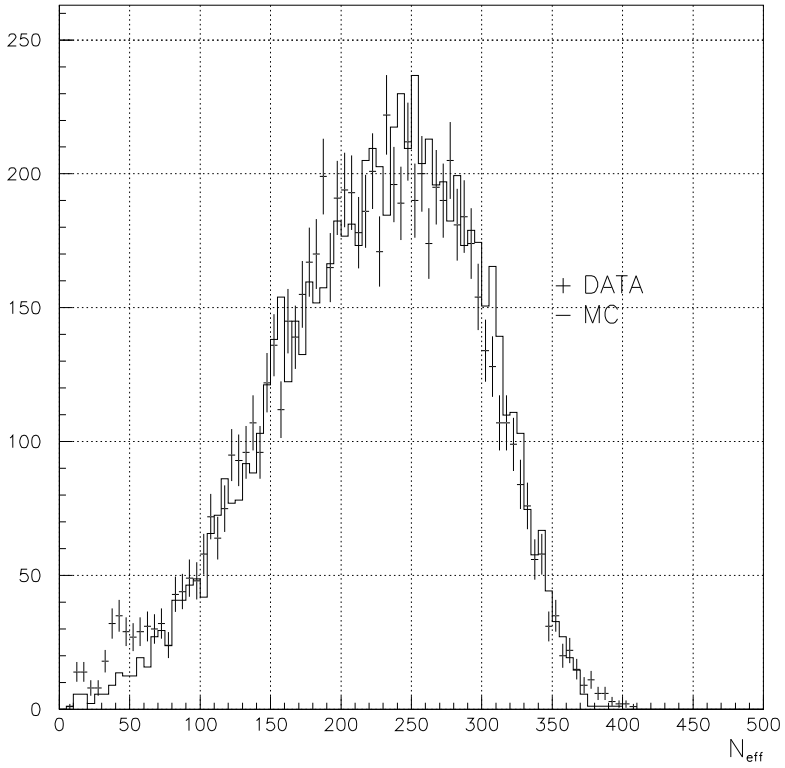

Figure 10.5: The Michel spectrum, solid line shows MC and cross shows data

Time difference cut

Since muon decay electron is successive phenomena after stopping muon, there is problem of trigger gate. The trigger time width in Super-Kamiokande detector is 800nsec. The gate type is classified for three groups because of the relation of muon and electron and gate type as Fig. 10.6. Only sub-gate events of which detection efficiency are highest, are used for this study. The types of trigger gate are explained as follows,

1. in-gate event
   The time difference between parent muon and decayed electron is very small. It is difficult for detection decay electron because of signal tail of parent muon.

2. bye-bye event
   The event decay electron signal is divided two gate.

3. sub-gate event
   After parent muon gate is finished, electron signal appears in the next gate.

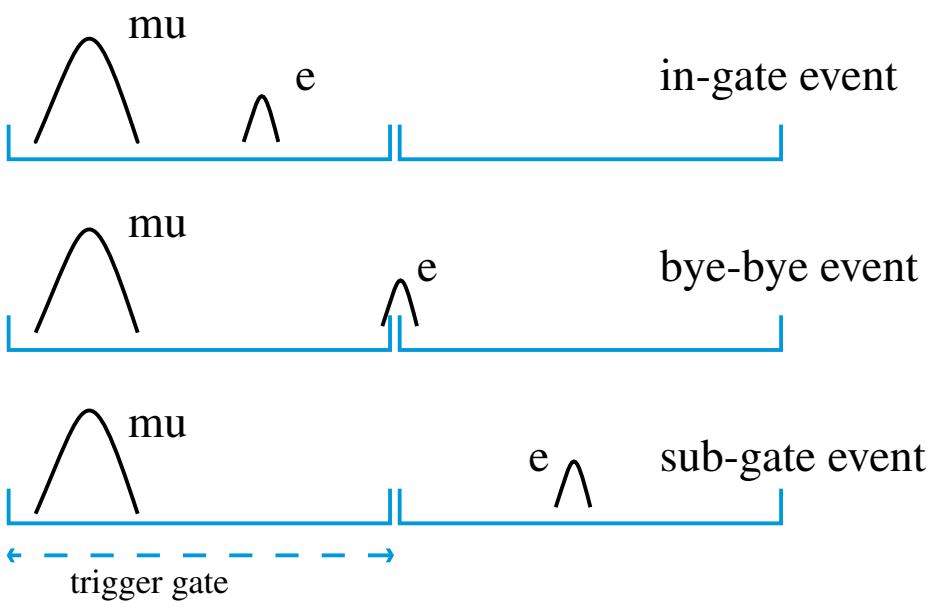

Figure 10.6: Schematic view of μ-e decay events for gate pulse

Detection efficiency for μ^+ decay e

The detection efficiency for μ^+ decay e is estimated by Monte Carlo simulation. The positive electron with Michelle energy spectrum is generated and applied the detector simulator, the figure is shown in Fig. 10.9. The goodness cut and low energy cut are applied, the detection efficiency for μ^+ decay e is estimated to be 98.7 ± 0.04stat.%.

10.4 Charge ratio of upward stopping muon

The 224 upward stopping muons are observed as parent muons and 114 decay electron which time difference between parent muons and decay electron is larger than 1.2μsec is observed. The ratio of number of electron tagged event to total muon is,

$$\frac{N_{e-tag}}{N_{total-\mu}} = \frac{114}{224} = 0.51 \pm 0.03(\text{stat.}) \tag{10.17}$$

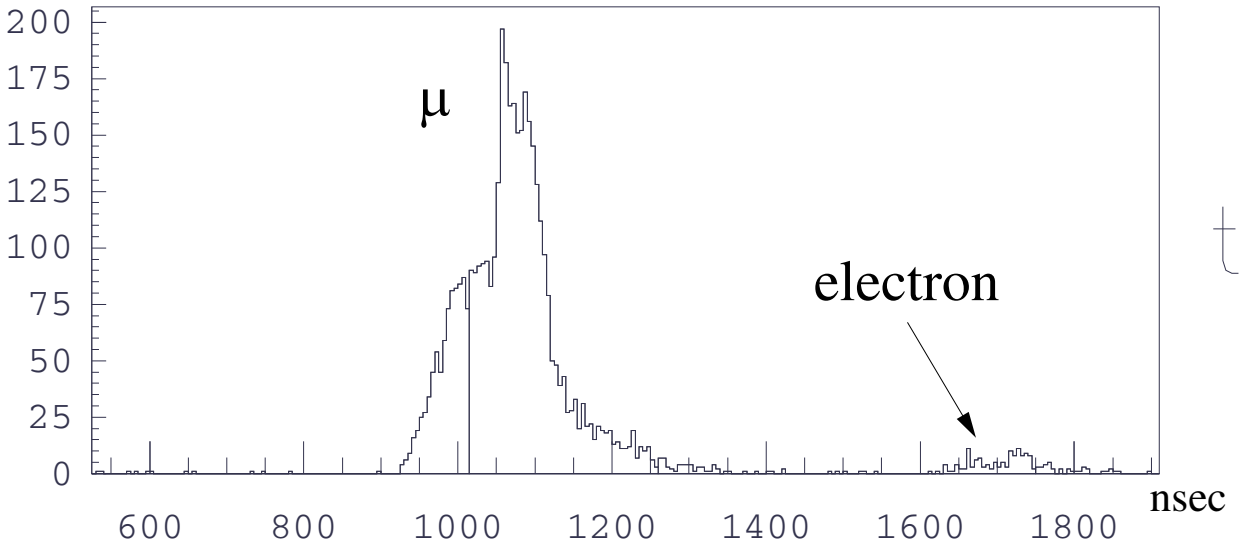

Figure 10.7: Timing distribution for in-gate event. Both parent muons and decay electron is available in the gate

Since equation(10.11), Equation(10.17), and the detection efficiency for μ^+ decay electron described as 10.3.2 are taken into account. The charge ratio for upward stopping muons($E_\mu \geq 1.4$GeV) is obtained to be

$$\frac{N_{\mu^-}}{N_{\mu^+}} = 0.57^{+0.78}_{-0.39}(\text{stat.}) \tag{10.18}$$

Figure 10.10 shows the relation between $N_{\text{e-tag}}/N_{\text{total}_\mu}$ and N_{μ^+}/N_{μ^-}.

10.5 Expected charge ratio

The expected charge ratio is estimated by the analytical calculation described as Chapter 7. The expected upward stopping muon flux from atmospheric ν_μ and $\bar{\nu_\mu}$ are 0.50 and 0.25 respectively. So the ratio of upward stopping muon flux from ν_μ to $\bar{\nu_\mu}$ is 1.98 obtained.

10.6 Systematic uncertainties

10.6.1 The systematic error for absolute energy determination

The energy distribution of μ decay electron is shown in Fig. 10.11. The cross shows data and the slid line shows Monte Carlo data, the difference is found in mean energy with

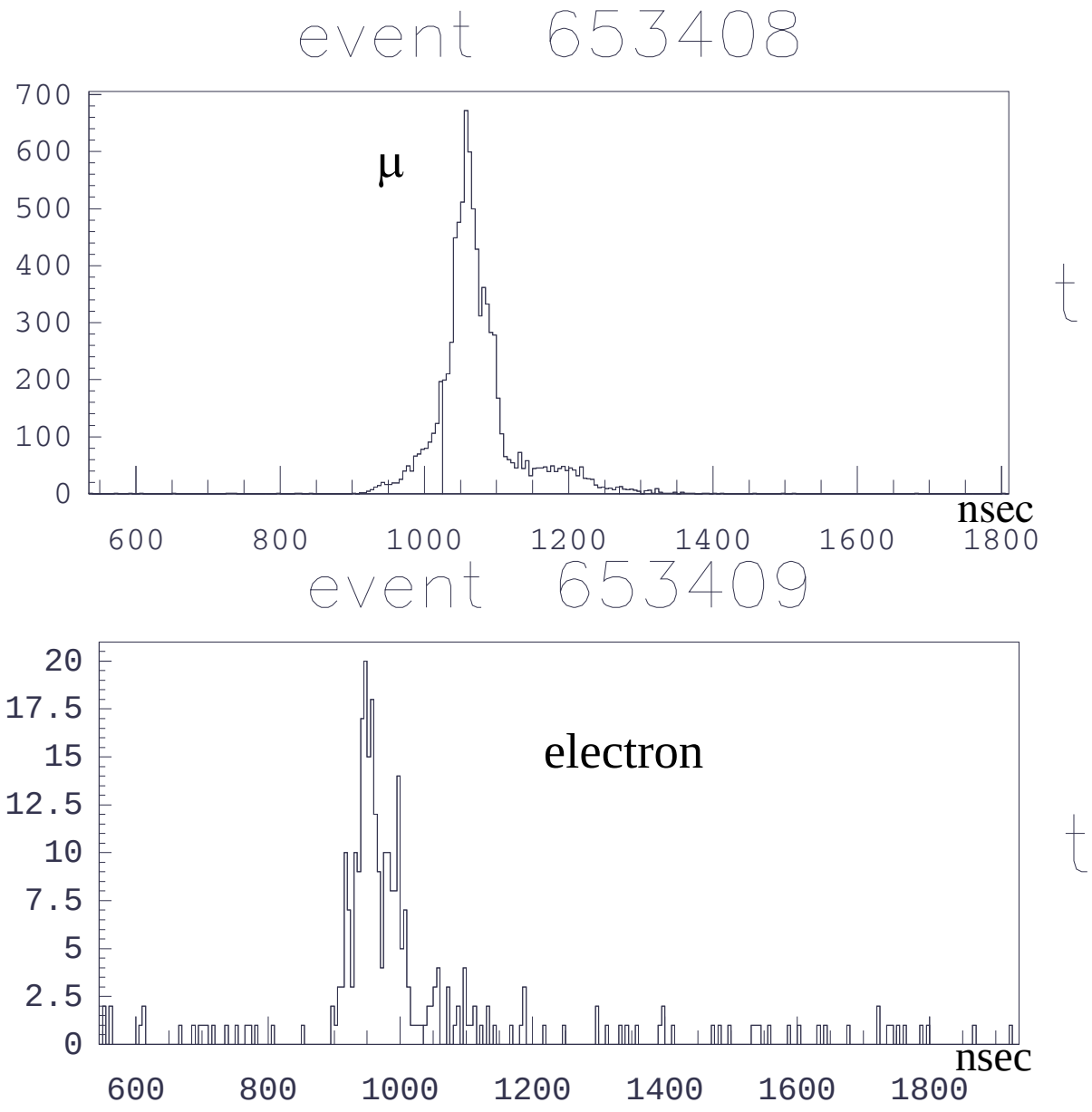

Figure 10.8: Timing distribution for sub-gate event. Upper figure shows parent muons and lower figure shows decay electron

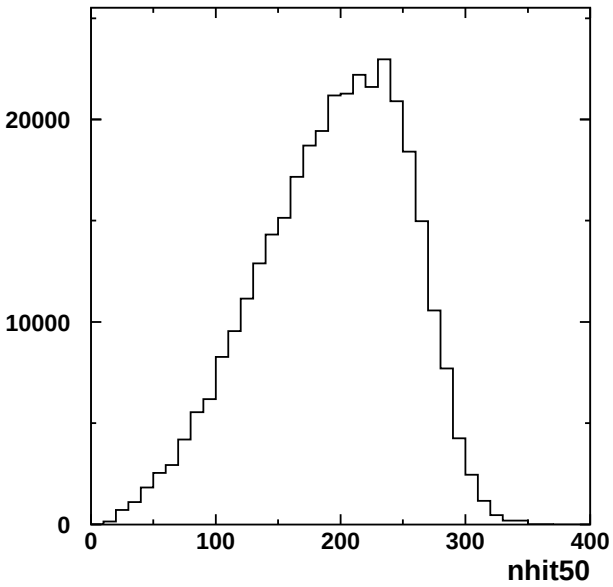

Figure 10.9: The Michelle spectrum of μ^+ decay e^+ generated by Monte Carlo simulation

2.5%. The difference of the mean energy affects to observed atmospheric $\nu_\mu/\bar{\nu_\mu}$ ratio with 13.2%.

Detection efficiency for μ^+ decay electron

The detection efficiency for μ^+ decay electron is estimated to be 98.7 ± 0.04stat.% in Section 10.3.2, the statistic error for detection efficiency affects to observed atmospheric $\nu_\mu/\bar{\nu_\mu}$ ratio with 0.6%.

The uncertainty of neutrino-nucleon interaction

The total neutrino-nucleon charged current cross section is shown in Fig. 10.12. The cross points show the various experimental results and the blue line shows the analytical calculation described in Section 7.3. The ν_μ and $\bar{\nu_\mu}$ data are independently fitted by analytical calculation ,respectively. The difference between expected ratio of $\sigma_{\nu N}$ to $\sigma_{\nu\bar{N}}$ and normalized theoretical ratio is estimated to be 8%. The effect for observed atmospheric $\nu_\mu/\bar{\nu_\mu}$ ratio is 8% obtained.

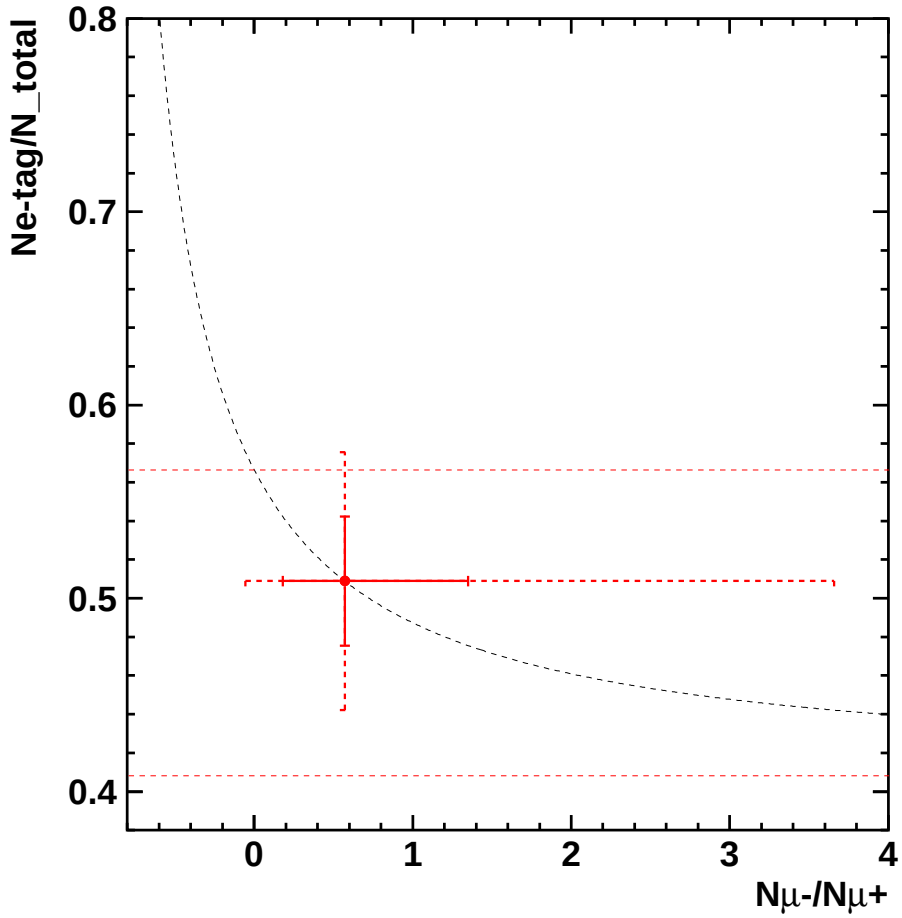

Figure 10.10: The $N_{\text{e-tag}}/N_{\text{total}_\mu}$ versus N_{μ^+}/N_{μ^-}

10.7 Obtained atmospheric $\nu/\bar{\nu}$

The ratio of observed atmospheric $\nu/\bar{\nu}$ to expected one is estimated as follows,

$$\frac{(\nu/\bar{\nu})_{obs.}}{(\nu/\bar{\nu})_{theo.}} = 0.29^{+0.39}_{-0.20}(\text{stat.}) \pm 0.04(\text{syst.}) \quad ^{+1.56}_{-0.16}(\text{stat.}2\sigma) \tag{10.19}$$

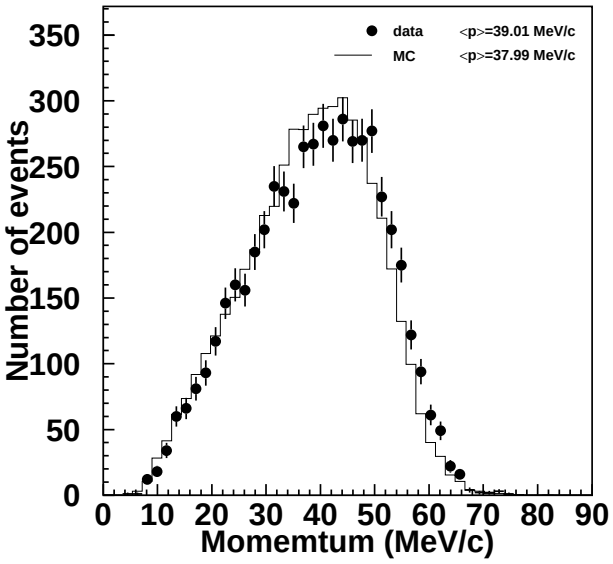

Figure 10.11: The energy distribution of μ decay electron

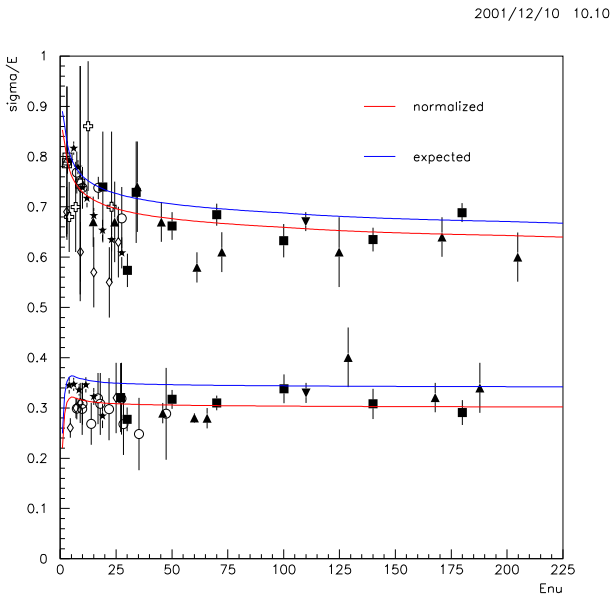

Figure 10.12: Neutrino-nucleon charged current cross section

Chapter 11

Result and discussions

The live time 1247 days for upward stopping muons and 1268 days for upward through-going muons data were studied, the 345 upward stopping muon events and 1416 upward through-going muon events were detected.

11.1 Observed upward-going muon flux

The observed upward-going muon flux was estimated from upward-going events. The observed upward stopping muon flux was $0.41 \pm 0.02(\text{stat.}) \pm 0.02(\text{syst.})$ ($\times 10^{-13}\text{cm}^{-2}\text{s}^{-1}\text{sr}^{-1}$), the through-going muon flux was $1.70 \pm 0.05(\text{stat.}) \pm 0.02(\text{syst.})$ ($\times 10^{-13}\text{cm}^{-2}\text{s}^{-1}\text{sr}^{-1}$), the stop/through ratio was $0.24 \pm 0.02(\text{stat.}) \pm 0.01(\text{syst.})$, total upward-going muon flux was $2.11 \pm 0.05(\text{stat.}) \pm 0.03(\text{syst.})$ ($\times 10^{-13}\text{cm}^{-2}\text{s}^{-1}\text{sr}^{-1}$) obtained.

11.2 Expected upward-going muon flux

The expected upward-going muon flux was estimated by analytical calculation on the basis of the Bartol atmospheric flux model, GRV94 parton distribution function for deep inelastic scatter, energy loss of muons calculated by Lohmann. The expected upward stopping muon flux was $0.73 \pm 0.16(\text{theo.})$ ($\times 10^{-13}\text{cm}^{-2}\text{s}^{-1}\text{sr}^{-1}$), through-going muon flux was $1.97 \pm 0.44(\text{theo.})$ ($\times 10^{-13}\text{cm}^{-2}\text{s}^{-1}\text{sr}^{-1}$), the ratio of stopping to through-going muon flux was $0.37 \pm 0.05(\text{theo.})$, the total upward-going muon flux was $2.70 \pm 0.47(\text{theo.})$ ($\times 10^{-13}\text{cm}^{-2}\text{s}^{-1}\text{sr}^{-1}$) obtained.

11.3 Oscillation examination

The oscillation examination was applied by comparison between the observed upward-going muon flux and the expected upward-going muon flux. The result of the oscillation examination is summarized in Table 11.1, where α, β, γ are described in Chapter8.

$\sin^2\theta$	Δm^2	χ^2/d.o.f	α	β	ϵ	Prob.(%)
stop/through ratio 5bin						
0.00	–	9.4/ 5	–	-0.3	–	9.4%
1.04	3.0×10^{-3}	1.3/ 3	–	0.0	–	71.8%
1.00	2.9×10^{-3}	1.4/ 3	–	0.0	–	71.2%
stop + through combined 15bin						
0.00	–	30.2/15	-0.2	-0.3	0.05	1.1%
1.02	3.2×10^{-3}	7.1/13	0.03	0.002	-0.01	89.6%
1.00	3.2×10^{-3}	7.1/13	0.03	-0.01	-0.004	89.5%
through 10bin						
0.00	–	18.7/10	-0.16	–	0.05	4.4%
0.86	5.2×10^{-3}	5.9/ 8	0.05	–	-0.001	66.1%

Table 11.1: The summary of oscillation analysis

11.4 Monte Carlo approach

The another approach for estimation upward going muon flux applied Monte Carlo method. The Bartol atmospheric neutrino flux model, GRV94 parton distribution function for deep inelastic scatter calculation, the energy loss of muon calculated by Lohmann were applied and the GEANT program in CERN library simulated the detector response. The upward-going muon fluxes were estimated by Monte Carlo method, the upward stopping muon flux was 0.73 ± 0.03(stat.) ($\times 10^{-13}$cm^{-2}s^{-1}sr^{-1}), the upward through-going muon flux was 1.98 ± 0.02(stat.) ($\times 10^{-13}$cm^{-2}s^{-1}sr^{-1}), the ratio of stopping muon flux to through-going was 0.39 ± 0.01(stat.) obtained.

11.5 Atmospheric $\nu_\mu/\bar{\nu_\mu}$ ratio

The experimental atmospheric $\nu_\mu/\bar{\nu_\mu}$ ratio was estimated by using the muon lifetime difference in the water.

The experimental charge ratio of negative muon to positive muon(N_{μ^-}/N_{μ^+}) was obtained to be $0.57^{+0.78}_{-0.39}$(stat.). and the ratio of observed $\nu_\mu/\bar{\nu_\mu}$ to expected from analytical calculation was estimated to be $0.29^{+0.39}_{-0.20}$(stat.) $\pm$ 0.04(syst.).

Chapter 12

Conclusion

The atmospheric neutrino flux has been measured using about 1250days exposure at the Super-Kamiokande detector. 345 events for upward stopping muons and 1416 events for upward through-going muons were detected. The experimental upward-going muon flux was obtained on the basis of the observed muons. The expected flux without neutrino oscillation was estimated by analytical calculation.

The oscillation examination was done by comparison between observed upward-going muon flux and expected one. The $\nu_\mu \to \nu_\tau$ vacuum oscillation is considered as the most probable process. The $\nu_\mu \to \nu_\tau$ oscillation hypothesis with $\sin^2 2\theta \geq 0.65, 1.9 \times 10^{-3} \leq \Delta m^2 \leq 7.2 \times 10^{-3}$ is consistent with the observed zenith angle shape at 90% confidence level. We obtained the probability of 89.5% at a best fit parameters at $(\sin^2 2\theta, \Delta m^2) = (1.0, 3.2 \times 10^{-3})$ for the $\nu_\mu \to \nu_\tau$ oscillation case. On the other hand, we obtained the probability of 1.1% for the null oscillation case. The Monte Carlo approach was applied for the realistic expected flux estimation and about 20years upward-going muon events were generated. The upward-going muon flux by Monte Carlo was compared with analytical calculation. Although the distribution of the zenith angle was consistent, the absolute value of the flux for through-going muon was found 4% difference.

The observed atmospheric $\nu_\mu/\bar{\nu_\mu}$ ratio was measured and the expected ratio was estimated by analytical calculation. The ratio of observed to expected was $0.29^{+0.39}_{-0.29}(\text{stat.}) \pm 0.04(\text{syst.})$ obtained.

bibliography

[1] K.S.Hirata et al.,Phys. Lett. B205(1988)416

[2] M.Takita, Ph.D.thesis, Fac. of Science, Univ. of Tokyo(1989),ICR-Report-186-89-3.

[3] D.Casper et al.,Phys. Rev. Lett. 66(1991)2561

[4] R,Beckser-Szendy et al., Phys.Rev. D46(1992)3720

[5] T.Kafka Talk at the TAUP 93 Conf., Gran Sasso,Sep.1993

[6] F.Ronga et al., Upward-going muons and MACRO, talk of neutrino '98(1998)

[7] Y.Fukuda et al., Phys. Lett. B335(1994)237

[8] Ch.Berger et al., Phys.Lett. B227(1989)489.

[9] N.Aglietta et al., Europhys.Lett. 8(1989)611.

[10] Z.Maki, M.Nakagawa and S.Sakata, Prog.Theor.Phys. 28(1962)870.

[11] B.Pontecorvo, Sov.Phys.JETP 26(1968)984.

[12] M.Ambrosio et al. INFN-AE-97-55,Nov. 1997

[13] V.Agrawal et al,. Phys.Rev. D53, 1314-1323, 1996

[14] L.V.Volkova, Yad.Fiz. 31(1980)1510 [Sov.J.Nucl.Phys. 31(1980)784].

[15] M.Honda and T.Kajita, K.Kasahara, S,Midorikawa, Phys.Rev. D52(1995)4985.

[16] A.V.Butkevitch, L.G.Dedenko and I.M.Zhelenznykh, Yad.Fiz. 50(1989)90 [Sov.J.Nucl .Phys. 50(1989)142].

[17] M.Glück, E.Reya and A.Vogt, Z.Phys. C67, 433-447, 1995

[18] W.Lohmann, R.Kopp and R.Voss, CERN Report No.85-03(1985) (unpublished).

[19] Review of Particle Properties, Particle Data Group, Phys.Rev., D50(1994)14

[20] T.Suzuki, D.F.Measday and J.P.Roalsvig, Phys.Rev., C35(1987)2212

[21] A. van der Schaaf et al., Nucl.Phys.A408(1983)573